

9 **Abstract**

10 Subantarctic Mode Water (SAMW) is examined using the data-assimilating, eddy-permitting
11 Southern Ocean State, for 2005 and 2006. Surface formation due to air-sea buoyancy flux is
12 estimated using Walin analysis, and diapycnal mixing is diagnosed as the difference between
13 surface formation and transport across 30°S, accounting for volume change with time. Water
14 in the density range $26.5 < \sigma_\theta < 27.1$ kg/m³ that includes SAMW is exported northward in
15 all three ocean sectors, with a net transport of (18.2, 17.1) Sv (for years 2005, 2006); air-sea
16 buoyancy fluxes form (13.2, 6.8) Sv, diapycnal mixing removes (-14.5, -12.6) Sv, and there
17 is a volume loss of (-19.3, -22.9) Sv mostly occurring in the strongest SAMW formation
18 locations. The most vigorous SAMW formation is in the Indian Ocean by air-sea buoyancy
19 flux (9.4, 10.9 Sv), where it is partially destroyed by diapycnal mixing (-6.6, -3.1 Sv). There
20 is strong export to the Pacific, where SAMW is destroyed both by air-sea buoyancy flux
21 (-1.1, -4.6 Sv) and diapycnal mixing (-5.6, -8.4 Sv). In the South Atlantic, approximately
22 the same volume of SAMW is formed by air-sea buoyancy flux (5.0, 0.5 Sv) as is destroyed
23 by diapycnal mixing (-2.3, -1.1 Sv). Peaks in air-sea flux formation occur at the Southeast
24 Indian and Southeast Pacific SAMWs (SEISAMW, SEPSAMW) densities. Formation over
25 the broad SAMW circumpolar outcrop windows is largely from denser water, driven by
26 differential freshwater gain, assisted or opposed by heating or cooling. In the SEISAMW
27 and SEPSAMW source regions, formation is from lighter water, driven by differential heat
28 loss.

1 Introduction

The Southern Ocean is a region of intense water mass transformation and formation, thus having a vital role in redistributing heat and freshwater in the global overturning circulation (Macdonald and Wunsch 1996; Sloyan and Rintoul 2001a,b; Talley et al., 2003; Talley, 2008). A major component of the Southern Ocean overturning circulation consists of the northward export of Subantarctic Mode Water (SAMW) and Antarctic Intermediate Water (AAIW) (McCartney, 1982; Rintoul, 1991; Sloyan and Rintoul, 2001b) which ventilates large areas of the lower thermocline in all three Southern Hemisphere oceans (Schmitz, 1996; Hanawa and Talley, 2001). These water masses play a significant role in Southern Hemisphere heat and freshwater transport, and also importantly impact the oceanic sink for tracers including anthropogenic CO₂ (Sabine et al., 2004) and chlorofluorocarbons (Willey et al., 2004).

SAMW and AAIW are formed by winter cooling of waters just to the north of the Subantarctic Front (SAF) and northward cross-frontal fluxes of Polar Zone surface water, which give rise to vertical convection on the equatorward flank of the SAF, the northernmost core of the Antarctic Circumpolar Current (ACC), resulting in deep winter mixed layers that dominate subtropical gyre ventilation to the north. McCartney (1977, 1982) was the first to describe and name these thick winter mixed layers. The associated winter mixed layer depths range from 200 m to 300 m in the Atlantic and western Indian Ocean to more than 500 m in the southeast Indian and Pacific Oceans (e.g. Dong et al., 2008). SAMW is the warmest in the western Atlantic (15 °C, 35.8 psu, 26.5 σ_θ) where the SAF is farthest equatorward, and coldest just west of Drake Passage (4-5°C, 34.2 psu, 27.1 σ_θ) where the SAF is farthest poleward. McCartney considered the densest SAMW in the southeastern Pacific and Scotia Sea to be the principal precursor of AAIW, the low salinity water mass that fills the Southern Hemisphere subtropical gyres and the tropical oceans at 800 m - 1000 m depth (Hanawa and Talley, 2001). This hypothesis was confirmed as part of an in situ study of SAMW and

54 AAIW formation in the southeast Pacific in 2005-2006 (Talley et al., 2006; Talley, 2007;
55 Holte, 2010; Holte et al., 2012; Holte et al., in preparation). This nearly point source of
56 AAIW, with only minor modifications due to mixing across the ACC at other longitudes,
57 stands in contrast to the near circumpolar formation of SAMW (McCartney, 1982; Rintoul
58 et al., 2001).

59 Despite the fundamental importance of SAMW/AAIW for global ocean circulation and
60 also for uptake of anthropogenic CO₂ (Sabine et al., 2004), the relative roles of differing
61 physical processes important for SAMW formation and destruction are still not completely
62 understood (e.g. Naveira Garabato, 2003; Sloyan and Kamenskovich, 2007). The complex mix
63 of processes affecting the SAMW source in the winter mixed layer includes air-sea buoyancy
64 fluxes, lateral circulation, Ekman and eddy-induced transport, and diapycnal mixing and
65 upwelling (e.g. Sallee et al., 2010; Sloyan et al., 2010; Holte et al., 2012). These same
66 processes govern air-sea CO₂ exchange. Using the high resolution (1/6° x 1/6°) Southern
67 Ocean State Estimate (SOSE; Mazloff et al., 2010), recent advances have been made toward
68 understanding the uptake and transport of anthropogenic CO₂, highlighting the importance
69 of SAMW formation in CO₂ subduction (Ito et al., 2010). The same SOSE solution is used
70 here to quantify the formation rate of SAMW and AAIW and export of these water masses
71 northward out of the Southern Ocean.

72 Transformation of water from one density class to another is driven by air-sea buoyancy
73 flux and diffusive processes (e.g. Tziperman, 1986); the formation of water in each density
74 class is given by the divergence of transformation with respect to density. Walin (1982)
75 developed a method to estimate water mass formation due to air-sea heat flux, assuming
76 that the error in ignoring diffusive diapycnal flux is no larger than the uncertainty in the air-
77 sea heat flux estimates. Walin's method was subsequently applied by Speer and Tziperman
78 (1992) and Speer et al. (1995) to estimate global-scale surface water mass formation rates
79 from observations.

80 The Walin (1982) method has been extended to include the effects of diapycnal mixing
81 using models (Garrett et al., 1995; Marshall et al., 1999; Nurser et al., 1999), and to estimate
82 global average diapycnal diffusivities implied by global-scale transformation, using observa-
83 tions (Zhang and Talley, 1998). Since diapycnal mixing is difficult to model and too weak
84 to observe directly, its local role in water mass transformation and formation is still poorly
85 quantified. Nevertheless, it has been shown that diapycnal mixing in the Southern Ocean
86 cannot be neglected (e.g. Speer et al., 2000; Sloyan and Rintoul, 2001a,b; Iudicone et al.,
87 2008a,c) especially over rough topography (e.g. Heywood et al., 2002; Naveira Garabato et
88 al., 2004, 2007), and is essential for water mass modification, especially when considering
89 the very large spatial scales of the global overturning circulation. We here quantify the
90 effects of diapycnal ocean mixing as the difference between the air-sea flux formation and
91 the meridional transport of SAMW out of the Southern Ocean, accounting for the internal
92 storage rate.

93 SOSE is particularly well suited to the problem of Southern Ocean water mass formation
94 because it: (i) is constrained to a large suite and number of oceanic observations, bringing
95 SOSE oceanic fields close to the observations (Mazloff et al., 2010). The optimization pro-
96 cedure used in SOSE greatly reduces the misfit between its estimates of temperature and
97 salinity and numerous observations (e.g. Argo profiling float data, the Southern Elephant
98 Seals as Oceanographic Samplers project, hydrographic sections) thus yielding a much more
99 accurate surface and interior density distribution (Mazloff et al., 2010); (ii) has the full spatial
100 and temporal resolution of a numerical model; (iii) has internally and dynamically consistent
101 oceanic fields and adjusted air-sea fluxes (evaluated in Cerovečki et al., 2011), so that they
102 exactly satisfy the ocean circulation model equations; and (iv) is an eddy-permitting model
103 that evolves rather than parameterizes eddy processes, which is especially important in the
104 Southern Ocean where the meridional overturning circulation in the SAMW density range
105 is believed to be a balance between the Eulerian mean flow and eddy-induced mean flow

106 (e.g. Karsten and Marshall, 2002) and is important given that many aspects of meridional
107 overturning circulation differ in coarse and high resolution models (Hallberg and Gnanade-
108 sikan, 2006; Spence et al., 2009). Eddy effects are also important in SAMW formation, as
109 eddy buoyancy supply can be comparable in magnitude to buoyancy supply by air-sea fluxes
110 (Cerovečki and Marshall, 2008).

111 We are using SOSE iteration 22, which provides a state estimate for years 2005 and 2006,
112 because Mazloff et al. (2010) has verified the high accuracy of its oceanic fields relative to
113 observations. (More recent SOSE iterations include a longer time period, which are being
114 used in subsequent work.)

115 In Section 2 the SOSE setup, its adjusted air-sea buoyancy fluxes and sea surface density
116 fields are presented, together with an outline of the methods. The spatial distribution and
117 properties of SAMW and AAIW in the 2005-2006 SOSE run are discussed in Section 3.
118 SAMW formation rates using Walin (1982) analysis with SOSE air-sea buoyancy fluxes and
119 sea surface density are presented in Section 4. For comparison, formation rates computed
120 using other commonly-used air-sea buoyancy flux products appear in the Appendix. In Sec-
121 tion 5, the effects of diapycnal mixing on SAMW formation and destruction are diagnosed as
122 the difference between the air-sea flux formation and the meridional transport of SAMW out
123 of the Southern Ocean, accounting for the internal storage rate. Discussion and conclusions
124 are provided in Section 6.

125 **2 Data sets and methods**

126 **2.1 Southern Ocean State Estimate (SOSE) and its air-sea fluxes**

127 The Southern Ocean State Estimate (SOSE) (Mazloff et al., 2010) provides a complete data
128 set including atmospheric forcing fields and three-dimensional oceanographic fields south of
129 24.7°S at 1/6° horizontal resolution.

130 SOSE utilizes an adjoint model (4D-Var method) to solve for the initial conditions and at-
131 mospheric state (air temperature, specific humidity, downwelling shortwave radiation, wind
132 velocity, and precipitation) required to bring the ocean circulation model results into con-
133 sistency with oceanic observations (see, for example, Stammer et al., 2004 or Wunsch and
134 Heimbach, 2007). The first guess oceanic initial conditions in SOSE are derived from and
135 constrained to the 1° resolution Ocean Comprehensible Atlas (OCCA) global state estimate
136 (Forget, 2010). The northern open boundary condition is also derived from OCCA. For the
137 initial atmospheric state estimate, as well as constraints, SOSE uses the National Centers for
138 Environmental Prediction-National Center for Atmospheric Research Reanalysis 1 (hereafter
139 NCEP1) (Kalnay et al., 1996). As described in Mazloff et al. (2010), the adjusted atmo-
140 spheric variables are combined with the Large and Pond (1981) bulk formulae to obtain the
141 air-sea heat and freshwater flux forcing fields. This bulk formulation is used for historical
142 reasons; the results are insensitive to this choice compared with more modern COARE bulk
143 formulae. We have already shown that SOSE estimates of atmospheric variables tend to
144 correct the NCEP1 biases documented by Taylor et al. (2000) (Cerovečki et al., 2011).

145 The SOSE net air-sea heat fluxes for 2005-2006 are shown in Figure 1. The most intense
146 ocean heat loss is over the subtropical western boundary currents. The ocean also loses heat
147 in the southernmost part of the Southern Ocean. The ocean gains heat over large regions of
148 the subtropical gyres in the Pacific and Indian Oceans. Robust regions of large (>50 W/m²)
149 ocean heat gain occur where cold polar waters flow northward beneath a more temperate
150 atmosphere (e.g. Large and Yeager, 2009, hereafter LY09), in the Malvinas Current east of
151 Drake Passage, and east of New Zealand where the Subantarctic Front is steered northward.
152 A significant band of heat gain that is unrelated to such northward flow is found in the
153 Indian Ocean between the Subantarctic and Subtropical Fronts, between 40 and 50°S, and
154 is also a feature of all of the other flux products compared here (Figure 2).

155 To compare the air-sea heat flux and freshwater flux contributions to buoyancy flux, we

156 convert freshwater and buoyancy fluxes to heat flux units of W/m^2 (e.g. Moore et al., 2002;
 157 Cerovečki et al., 2011). We express freshwater flux as the *freshwater heat-equivalent flux*
 158 defined by

$$159 \quad Q_{FW} = -\rho_0 \beta S c_p (E - P) / \alpha, \quad (1)$$

160 where ρ_0 is a reference density, S is salinity, c_p is the specific heat for seawater, E is evapo-
 161 ration, P is precipitation (E, P in m/s), β is the saline contraction coefficient, and α is the
 162 thermal expansion coefficient (as in Gill, 1982), and positive flux results in increased buoy-
 163 ancy (decreased density) (opposite of Gill’s convention). A heat flux contribution of $1 \text{ W}/\text{m}^2$
 164 to ocean buoyancy flux is equivalent to $1 \text{ mg}/(\text{m}^2 \text{ sec})$ freshwater flux, or $\sim 3.1 \text{ cm}/\text{year}$ of
 165 E-P at 5°C (Large and Nurser, 2001). The *buoyancy heat-equivalent flux* is the sum of the
 166 net air-sea heat flux and freshwater heat-equivalent flux. Positive heat/freshwater/buoyancy
 167 flux implies a decrease in surface density (an increase in surface buoyancy).

168 The SOSE freshwater heat-equivalent flux (Figure 1d-f) shows net evaporation in the
 169 subtropical gyre and net precipitation in higher latitudes. The freshwater flux contribution
 170 to the buoyancy flux becomes increasingly important in higher latitudes due to nonlinearity
 171 in the equation of state (Moore et al., 2002). Thus, in the cold waters of the polar latitudes,
 172 the freshwater flux contribution is the same order as or larger than the heat flux contribution;
 173 the two reinforce each other in the broad heat gain regions of the ACC, while in regions of
 174 cooling, the freshwater and heat contributions to buoyancy flux may nearly cancel (Figure 1g-
 175 i) (e.g. Warren et al., 1996; Speer et al., 2000). As a result, different air-sea buoyancy flux
 176 products can even differ in sign in polar latitudes because of varying small biases in either
 177 flux (e.g. Taylor et al., 2000; Cerovečki et al., 2011). Significant discrepancies are evident
 178 in Figure 2 where the NCEP1 ocean buoyancy gain in polar latitudes (average for years
 179 2005-2006) is much stronger than in the ERA-Interim Reanalysis of the European Centre
 180 for Medium-Range Weather Forecasting’s (ECMWF), the Large and Yeager (2009) flux

181 product, and SOSE, whereas OCCA is characterized by ocean buoyancy loss rather than
182 gain. These result in differing Walin formation rate estimates for the various flux products
183 (see Appendix), highlighting the importance of using air-sea fluxes that are consistent with
184 the interior ocean properties, e.g. SOSE.

185 **2.2 Formation rate estimates**

186 The density of a water parcel is predominantly changed at the sea surface through air-
187 sea buoyancy fluxes, but it can also be changed in the interior through the usually weaker
188 diapycnal fluxes associated with mixing. Surface SAMW formation in SOSE is estimated
189 using the “Walin” approach (Section 4). The SOSE velocity and density fields are then used
190 to calculate net meridional export or import of water in isopycnal layers across 30°S, zonal
191 transports between the ocean basins, and the net storage rate in isopycnal layers during the
192 two-year run (2005-2006) (Section 5). Finally, the formation rate due to diapycnal mixing
193 is diagnosed as the difference between the surface formation and the sum of the export and
194 interior storage rate (Section 5.3).

195 Our analysis is carried out only for densities lower than the densest variety of SAMW
196 ($\sigma_\theta = 27.1 \text{ kg/m}^3$) because the simplified sea-ice model in this SOSE iteration reduces
197 confidence in transports for higher densities that outcrop in the sea-ice zone south of the
198 Polar Front. Because of our cutoff at $\sigma_\theta = 27.1 \text{ kg/m}^3$, the isopycnal layers are shallower
199 than $\sim 1000\text{m}$, and we can use potential density relative to the sea surface to approximate
200 neutral surfaces.

201 **2.2.1 Walin method**

202 Walin’s (1982) method quantifies the rate at which water is added to or destroyed within
203 a specific density class. This “formation rate” is given by the divergence with respect to
204 density of the “transformation rate”, which is the rate at which water is transformed from

205 one density class to another via a diapycnal volume flux A either at the sea surface or in
 206 the interior of the ocean. In an inviscid, incompressible fluid, the transformation rate (A)
 207 depends only on the non-advective buoyancy supply to the volume considered, while the
 208 advective supply of buoyancy only deforms the bounding material surface without changing
 209 the volume. Following Garrett et al. (1995) and Marshall et al. (1999), the transformation
 210 rate A is

$$211 \quad A = F(\sigma, t) - \frac{\partial D}{\partial \sigma} \quad (2)$$

212 where $F(\sigma, t)$ is the net air-sea buoyancy flux integrated over the outcrop window bounded
 213 by isopycnal surfaces $\sigma \pm \frac{1}{2}\Delta\sigma$ (next subsection), and D is the diapycnal buoyancy flux with
 214 diapycnal divergence $\partial D/\partial\sigma$. The water mass transformation rate A has units m^3/s .

215 2.2.2 Surface formation rates estimated using the Walin method

216 The buoyancy flux B is given by (e.g. Gill, 1982)

$$217 \quad B = \frac{g}{\rho_0} \left[\frac{\alpha Q_{net}}{c_p} - \rho_0 \beta S(E - P) \right] \quad (3)$$

218 where Q_{net} is the net surface heat flux (positive for ocean heat gain). Positive buoyancy flux
 219 implies an increase in surface buoyancy (a decrease in surface density). (The sign convention
 220 is opposite that of Gill.) The associated transformation rate $F(\sigma, t)$ due to air-sea buoyancy
 221 flux within the density layer bounded by isopycnal surfaces $\sigma \pm \frac{1}{2}\Delta\sigma$ is given by:

$$222 \quad F(\sigma, t) = \frac{\rho_0}{g \Delta\sigma} \iint_{\mathcal{A}_S(\sigma, t)} B \delta_T(\sigma', \Delta\sigma) d\mathcal{A}', \quad (4)$$

224 in which $\mathcal{A}'(\sigma, t)$ is the instantaneous surface bounding the volume within which the density
 225 is $\sigma \pm \frac{1}{2}\Delta\sigma$, ρ_0 is the reference surface density, g is gravitational acceleration, and $\delta_T(\sigma', \Delta\sigma)$
 226 is a top-hat function of σ' which is zero except in the interval $\sigma \pm \frac{1}{2}\Delta\sigma$, where it has unit value
 227 (see e.g. Speer and Tziperman, 1992; Marshall et al., 1999). This equation holds for time

228 dependent as well as steady flows (e.g. Marshall et al., 1999) because \mathcal{A}' is the instantaneous
 229 bounding surface. Positive F corresponds to transformation towards increasing density.

230 The net water mass formation (destruction) rate \mathcal{FR} due to air-sea buoyancy fluxes in
 231 the density layer $\sigma \pm \frac{1}{2}\Delta\sigma$ is obtained as the difference of the transformation rates at the
 232 two isopycnal surfaces bounding this isopycnal layer:

233

$$234 \quad \mathcal{FR} = F\left(\sigma + \frac{\Delta\sigma}{2}\right) - F\left(\sigma - \frac{\Delta\sigma}{2}\right) \quad (5)$$

235 where \mathcal{FR} also has units m^3/s .

236 **2.2.3 Formation rates by diapycnal mixing**

237 Calculation of water mass formation rates using air-sea fluxes alone, following Walin’s (1982)
 238 approach, ignores diapycnal processes (e.g. Eq. (2)). At the largest global spatial scales, the
 239 isopycnal layers are completely closed at the surface, and any net formation or destruction
 240 by air-sea fluxes at the sea surface must be balanced by diapycnal processes. Calculation of
 241 these rates yields a diagnosis of globally-averaged diapycnal diffusivity for the given isopycnal
 242 (e.g. Zhang and Talley, 1998). Because SOSE provides consistent air-sea fluxes, velocity, and
 243 temperature/salinity fields, and includes the relevant diapycnal processes, we can estimate
 244 the effect of diapycnal processes by quantifying the proportion of SAMW that is formed
 245 (or destroyed) in the ocean interior, separate from air-sea fluxes. To do this, we calculate
 246 the volume transport between the Southern Ocean and the rest of the ocean across 30°S
 247 (Section 5.1), and the internal storage in isopycnal layers (Section 5.2), which is non-zero
 248 because the SOSE run is only two years and the system is not in steady state. The difference
 249 between the air-sea flux formation rate and the export of water in a given density range
 250 corrected for internal storage is equal to the rate of gain or loss due to diapycnal mixing
 251 (Section 5.3).

252 Volume transport \mathcal{V} in isopycnal layers across a vertical section is calculated as:

$$253 \quad \mathcal{V}(\sigma_\theta \pm \frac{\Delta\sigma}{2}) = - \iint_{\sigma_\theta \pm \frac{\Delta\sigma}{2}} v \, dA \quad (6)$$

254 where σ_θ is potential density anomaly referenced to the surface, v is the velocity component
 255 perpendicular to the section, and dA is the area of the vertical section bounded above and
 256 below by the isopycnals $\sigma_\theta \pm \Delta\sigma/2$. \mathcal{V} has units m^3/s . In our calculation the width of density
 257 bins $\Delta\sigma$ is $0.1 \text{ kg}/\text{m}^3$. Both v and σ_θ are five day averages of SOSE output.

258 The interior storage rate $\partial V(\sigma_\theta \pm \frac{\Delta\sigma}{2}, t)/\partial t$ for each of the two years is the change in vol-
 259 ume V of each isopycnal layer from the beginning to the end of each year of the SOSE simula-
 260 tion. Finally, the rate of formation or destruction due to diapycnal mixing $\partial^2 D(\sigma_\theta \pm \frac{\Delta\sigma}{2})/\partial\sigma^2$
 261 (from Eqs. (2) and (5)) is estimated considering the volume budget of each density layer
 262 $\sigma_\theta \pm \frac{1}{2}\Delta\sigma$:

$$263 \quad \frac{\partial V(\sigma_\theta \pm \frac{\Delta\sigma}{2})}{\partial t} = \mathcal{V}(\sigma_\theta \pm \frac{\Delta\sigma}{2}) + \mathcal{FR} + \mathcal{DR}, \quad (7)$$

264 where $\partial V(\sigma_\theta \pm \frac{\Delta\sigma}{2}, t)/\partial t$ is the storage rate, $\mathcal{V}(\sigma_\theta \pm \frac{\Delta\sigma}{2}, t)$ is the volume transport in (or
 265 out of) the same isopycnal layer in the relevant ocean sector (meridionally across 30°S and
 266 zonally into and out of the ocean sector) (Eq. 6), where positive (negative) transport is into
 267 (out of) the relevant ocean sector, and \mathcal{FR} is formation by air-sea fluxes (Eq. (5)). \mathcal{DR} is
 268 the diapycnal mixing equivalent to \mathcal{FR} , and, from Eqs. (2) and (5), is given by

$$269 \quad \mathcal{DR} = \frac{\partial D}{\partial\sigma}(\sigma + \frac{\Delta\sigma}{2}) - \frac{\partial D}{\partial\sigma}(\sigma - \frac{\Delta\sigma}{2}). \quad (8)$$

270 Since the terms comprising D have not been archived for the SOSE simulation analyzed
 271 here, we can calculate the net formation/removal rate \mathcal{DR} due to the diapycnal mixing from
 272 Eq. (8), but cannot determine the dynamical source of the mixing (e.g., boundary layer
 273 dynamics, eddy stirring, wave breaking, wind mixing).

274 3 SAMW spatial distribution and properties

275 Before estimating the formation rates, we examine the distribution of SAMW (and AAIW)
 276 in SOSE. The high spatial resolution of SOSE provides much greater detail than previously-
 277 published maps based on hydrographic profile data; the bulk SAMW properties in SOSE are
 278 comparable to previously-published descriptions.

279 Mode water is a thick layer of nearly homogeneous water extending over a large area,
 280 usually situated between the seasonal and the main pycnoclines (e.g. Hanawa and Talley,
 281 2001). Because of its vertical homogeneity, mode water is characterized by low potential
 282 vorticity (PV). Neglecting relative vorticity, PV is:

$$283 \quad PV = (f/\rho_\theta)\partial\rho_\theta/\partial z, \quad (9)$$

284 where f is the Coriolis parameter and $\rho_\theta = \sigma_\theta + 1000 \text{ kg/m}^3$ is the potential density. The
 285 PV values that define the boundaries of specific mode waters in the literature are generally
 286 obtained empirically from observations. Following their eastward evolution along the ACC,
 287 we describe the Indian and then the Pacific Ocean SAMW distributions, and then briefly the
 288 South Atlantic's much weaker (relatively high PV) SAMW (e.g. McCartney, 1982; Hanawa
 289 and Talley, 2001).

290 **a) Indian Ocean.** Mode Water properties overall in the south Indian Ocean range
 291 from $\sigma_\theta = 26.5$ to 26.9 kg/m^3 , including both Subtropical Mode Water and SAMW (Fine,
 292 1993; Wong, 2005). Two major types of SAMW are identified: a lighter and less well-
 293 developed SAMW (relatively higher PV) in the west, with $\sigma_\theta = 26.70 \text{ kg/m}^3$, originating
 294 in the Subantarctic Zone between 70° - 80°E , and a stronger (lower PV) type of SAMW
 295 in the east, with $\sigma_\theta=26.85 \text{ kg/m}^3$, originating in the Subantarctic Zone between 100° -
 296 110°E (McCartney, 1982) (Figures 3e and 4b). The denser SAMW is the southeast Indian
 297 SAMW (SEISAMW), which originates from especially deep mixed layers. After subduction
 298 it remains the most well developed and pervasive mode water in the Indian Ocean, and in

299 fact is one of the dominant mode waters of the global ocean (e.g. McCarthy and Talley,
300 1999; Hanawa and Talley, 2001).

301 Deep winter mixed layers north of the Subantarctic Front, which are the source of SAMW,
302 deepen towards the east in the Indian Ocean (evident in the Dong et al. (2008) climatology
303 superimposed in Figs. 3 and 4), with an especially large increase east of Kerguelen plateau,
304 becoming more than 500-550 m deep south of Tasmania. Using the 95% oxygen saturation
305 depth as proxy for the mixed layer depths, Talley (1999) showed an abrupt onset of high
306 oxygen and deep mixed layers in the central Indian Ocean east of Kerguelen Plateau, at
307 $\sim 80^\circ\text{E}$, $50\text{-}60^\circ\text{S}$. Very low PV in the annual mean SOSE solution coincides with these very
308 deep austral winter mixed layers (Figures 3f and 4a).

309 In SOSE the very low PV of SEISAMW is well depicted, as is the congruence between the
310 location of lowest PV on the representative SEISAMW isopycnals $\sigma_\theta=26.75$ and 26.8 kg/m^3
311 and the location of deep winter mixed layers north of the Subantarctic Front (from Dong
312 et al., 2008) (Figures 3f and 4a). The low PV distribution on the $\sigma_\theta=26.8$ surface closely
313 resembles that shown in McCarthy and Talley (1999), with PV values of about 40×10^{-12}
314 $(\text{m s})^{-1}$.

315 The SOSE representation of SEISAMW potential temperature and salinity (Figure 5)
316 is consistent with Thompson and Edwards (1981), Talley (1999) and Dong et al. (2008),
317 among others. Thompson and Edwards (1981) observed winter formation of SEISAMW with
318 potential temperature $8\text{-}9^\circ\text{C}$, salinity 34.55 , and $\sigma_\theta = 26.85\text{ kg/m}^3$. For comparison, at $\sigma_\theta =$
319 26.8 and 26.9 kg/m^3 , SOSE potential temperature is $8\text{-}9^\circ\text{C}$ and salinity is $34.6\text{-}34.7$.

320 **b) Pacific Ocean.** As originally described in McCartney (1977), SAMW density in-
321 creases progressively eastward from the western Indian Ocean to the southeast Pacific Ocean,
322 where the southeast Pacific SAMW (SEPSAMW) is formed (Figure 4e,f from SOSE). SEP-
323 SAMW is the densest variety of SAMW. The lowest values of PV associated with the global
324 distribution of SAMWs, less than $\sim 20 \times 10^{-12} (\text{m s})^{-1}$, are found in the southeast Pa-

325 cific. Low PV values and deep winter mixed layers result from strong wintertime convection,
 326 which was observed directly in 2005 (e.g. Sloyan et al., 2010; Holte et al., 2012). McCart-
 327 ney (1977, 1982) and Piola and Georgi (1982) showed that SEPSAMW lies in the σ_θ range
 328 27.05-27.1 kg/m³. In SOSE, the lowest PV, characteristic of SEPSAMW at $\sigma_\theta=27.0$ kg/m³,
 329 lies west of the southwest corner of Chile and protrudes northwestward into the subtropical
 330 gyre (Figure 4e,f), reflecting subduction and advection.

331 On all isopycnals in Fig. 6, the lowest salinity is in the southeastern Pacific east of
 332 $\sim 120^\circ\text{W}$, where PV is also lowest. The lowest PV is at $\sigma_\theta = 27.0$ and 27.1 kg/m³, marking
 333 the SEPSAMW (Figure 6e,f), which is the densest SAMW. Its potential temperature and
 334 salinity are 4-6°C and 34.0-34.3, consistent with the 4°-5°C and salinity of 34.2 summarized
 335 by Hanawa and Talley (2001). The associated isopycnal depths of 600-700m agree with the
 336 inferred maximum depth of convection of more than 600 m in this region based on oxygen
 337 (Tsuchiya and Talley, 1998); mixed layer depths of 550 m were observed directly in winter
 338 2005 (Holte et al., 2012). This coldest, freshest and densest SAMW is associated with AAIW
 339 (McCartney, 1977), which is the vertical salinity minimum of the Southern Hemisphere. A
 340 portion of AAIW subducts northward into the South Pacific subtropical gyre and a portion
 341 of AAIW proceeds eastward into the Drake Passage (McCartney, 1982; Talley, 1996).

342 The eastward increase of SAMW density from the western Indian to the eastern South Pa-
 343 cific is also evident in vertical sections of PV at various latitudes (Figure 7). The SEISAMW
 344 low PV pool at $\sigma_\theta = 26.8$ kg/m³ extends eastward from south of Australia to the central
 345 South Pacific, whereas the SEPSAMW low PV pool at $\sigma_\theta = 27.0$ kg/m³ is located west of
 346 Chile.

347 *c) Atlantic Ocean.*

348 In comparison with the Indian and South Pacific, the South Atlantic forms only lighter
 349 mode waters, centered at $\sigma_\theta = 26.5$ to 26.7 kg/m³ (Figure 3b-c), and concentrated in the
 350 southwest; these have been considered to be either Subantarctic Mode Water associated with

351 the multiple fronts of the Malvinas-Brazil Current and the Subantarctic Front (McCartney,
 352 1977, 1982; Tsuchiya et al., 1994) or Subtropical Mode Waters associated with the Brazil
 353 Current (Provost et al., 1999). The South Atlantic mode waters are much weaker (higher
 354 PV) than the Indian or South Pacific SAMWs, as seen from the weaker low PV pool on
 355 these isopycnals (Figure 3a-e).

356 The ridge of low PV in the Atlantic at $\sigma_\theta = 27.0$ to 27.3 kg/m^3 in Figure 7b, c is the
 357 SEPSAMW/AAIW from the southeastern Pacific, which is modified by air-sea buoyancy
 358 fluxes and mixing through the Drake Passage and the Malvinas Current. The result is a
 359 cooler, fresher and denser variety of AAIW in the Atlantic compared with the Pacific (e.g.
 360 Piola and Georgi, 1982; Talley, 1996), which is also evident in our Figure 6f.

361 4 SAMW transformation and formation by air-sea buoy- 362 ancy fluxes

363 To estimate global SAMW formation by air-sea buoyancy fluxes, we use the five-day aver-
 364 aged air-sea buoyancy flux and sea surface density fields from SOSE (south of 24.7°S , years
 365 2005 and 2006, considering $\sigma_\theta < 27.1$ kg/m^3) as input in the Walin analysis (Section 2.2.1).
 366 The buoyancy flux was integrated over the individual five-day averaged outcrop windows
 367 (Eq. (4)), with outcrop windows of width $\Delta\sigma = 0.1$ kg/m^3 . These five-day average trans-
 368 formation rate estimates were subsequently averaged over one year. Formation rates were
 369 then calculated as the difference of the transformation rates at the two isopycnal surfaces
 370 bounding each isopycnal layer (Eq. (5)). Throughout this section, rates are reported in pairs,
 371 for year 2005, followed by the estimate for year 2006.

372 We first estimate global transformation and formation rates for the entire Southern Ocean
 373 (Section 4.1, considering the isopycnal outcrops that cover not only the deep mixed layer
 374 regions where the low PV SAMWs originate but also all of the remaining circumpolar regions.
 375 We refer to these global calculations as “formation in the SEISAMW/SEPSAMW density

range”. To diagnose regional processes, we secondly consider transformation and formation in individual ocean sectors, integrating the air-sea fluxes in each ocean, and adjusting the rates for the zonal transports between the ocean sectors within the isopycnal layers. Divisions between the oceans are taken at 150°E, 70°W, and 20°E. In both the global and regional estimates we consider isopycnal outcrop windows 0.1 kg/m³ wide, centered at the SEISAMW density ($26.75 < \sigma_\theta < 26.85$ kg/m³), SEPSAMW density ($26.95 < \sigma_\theta < 27.05$ kg/m³), and South Atlantic SAMW density ($26.45 < \sigma_\theta < 26.55$ kg/m³). Finally, to better describe the flux processes in the lowest PV/deepest mixed layer regions and which are therefore associated with SAMW formation per se, we describe the geographic distribution of transformation and formation using maps (Section 4.6).

4.1 General features of SAMW transformation and formation by surface heat and freshwater fluxes

The most important feature of the annually averaged transformation rates is ocean buoyancy loss (becoming more dense, with positive transformation rates) at lower densities and buoyancy gain (becoming less dense with negative transformation rates) at the higher densities shown in Figure 8a,c,e. At the lower densities, which outcrop in the subtropics, the net buoyancy loss was predominantly due to ocean heat loss, although net evaporation also contributed. In the SAMW density range (26.5 - 27.1 kg/m³), freshwater input (net precipitation) contributed to buoyancy gain in both years, but the heat flux changed sign: net heat loss in 2005, and net heat gain in 2006. As a result, in 2005, the ocean lost buoyancy at densities up into the SAMW range $\sigma_\theta < 26.85$ kg/m³, while in 2006 ocean buoyancy loss was confined to densities lighter than $\sigma_\theta = 26.1$ kg/m³. In both years, freshwater gain was principally responsible for buoyancy gain at higher SAMW densities, although heat gain also contributed in 2006. This counterintuitive result, that even at these high latitudes buoyancy gain due to both freshwater and heat gain is integral to global (circumpolar) transformation

401 of water in the SAMW density range, has been described previously (Speer et al., 2000;
402 Sloyan and Rintoul, 2001a; Saltee et al., 2010).

403 Formation occurred in both years throughout the SAMW density range. The largest
404 rates, at $\sigma_\theta = 26.8 \text{ kg/m}^3$ and 27.0 kg/m^3 , correspond to SEISAMW and SEPSAMW (Sec-
405 tion 3) (Figure 8b,d,f). There were also smaller formation peaks at $\sigma_\theta=26.5 \text{ kg/m}^3$ and
406 26.2 kg/m^3 , corresponding to South Atlantic SAMW and Subtropical Mode Water. Both
407 freshwater fluxes and heat fluxes contributed to the formation. Because of monotonically
408 larger freshwater gain with increasing density (i.e. farther poleward), differential freshwater
409 input to the ocean contributed to formation throughout the SAMW density range. In gen-
410 eral, SAMW formation due to freshening was comparable in magnitude to SAMW formation
411 due to heat flux (which was both positive and negative).

412 4.2 Formation in the SEISAMW density range

413 Globally the net formation by air-sea buoyancy fluxes for the narrow SEISAMW density
414 range $\sigma_\theta=26.75\text{-}26.85 \text{ kg/m}^3$ was (5.6, 8.2) Sv (Figure 8 and Table A1). In both years,
415 freshwater gain was stronger at higher densities so that more (denser) water was transformed
416 into the SEISAMW range than was transformed out of the range, yielding (1.8, 4.0) Sv of
417 the total SEISAMW formation in (2005, 2006). Heat flux contributed to formation in both
418 years, but for different reasons: in 2005, 3.8 Sv were formed from excess ocean heat loss of
419 lighter waters relative to denser waters, and in 2006, 4.2 Sv were formed by excess ocean
420 heat gain from denser waters relative to lighter waters.

421 Regionally, when Walin integration is performed only over the Indian Ocean sector with
422 adjustment for isopycnal layer transport into and out of the sector, we still find that water
423 in the SEISAMW density range was formed from denser water through buoyancy gain in
424 both years. But within just the very lowest PV region indicating the source region of the
425 true mode water, formation maps (Section 4.6) show that buoyancy loss (due to cooling)

426 dominates the formation locally, in both years. This comparison illustrates the high regional
427 variability emphasized e.g. by Saltee et al. (2010).

428 **4.3 Formation in the SEPSAMW density range**

429 Globally, in both years, water in the SEPSAMW density range $\sigma_\theta=26.95\text{-}27.05\text{ kg/m}^3$ was
430 formed through buoyancy gain from denser water. In 2005, freshening and cooling con-
431 tributed 3.6 Sv and 2.7 Sv, respectively. In 2006, freshening formed 4.0 Sv, while 0.8 Sv
432 were destroyed by heat gain. The net formation was 6.3 Sv in 2005 and 3.2 Sv in 2006
433 (Figure 8 and Table A1).

434 In contrast to this global estimate, SEPSAMW within the Pacific ocean sector, as well
435 at its lowest PV source region (Section 4.6), was predominantly formed from lighter water
436 by buoyancy loss due to cooling. This is also true for the full SAMW density range within
437 the Pacific (Figure 9).

438 **4.4 Formation in the South Atlantic SAMW density range**

439 Winter mixed layers are much shallower in the Atlantic sector of the Southern Ocean than
440 in the Indian and Pacific sectors, resulting in weaker South Atlantic SAMW (Figure 3a-e)
441 (Tsuchiya et al., 1994; Provost et al., 1999). The global formation rates have a peak in 2006
442 (but not in 2005) at the density of South Atlantic mode water ($\sigma_\theta = 26.5\text{ kg/m}^3$)(Figure 8).
443 In 2006, this formation was from denser waters converted to SAMW through freshening and
444 heat gain that were both more intense at higher densities.

445 Regionally, when the Walin integration is performed only for the Atlantic sector, with
446 corrections for isopycnal layer transports in and out of the sector, the result is similar:
447 formation of South Atlantic SAMW from denser water through buoyancy gain (Figure 9).

448 4.5 Comparison with recent global Walin formation rate estimates

449 The overall pattern of buoyancy gain (rather than buoyancy loss) due to freshening, and to
 450 a lesser extent heat gain, over the SAMW outcrop windows agrees with numerous previous
 451 studies (Speer et al., 2000; Karstensen and Quadfasel, 2002; Saltee et al., 2010). We com-
 452 pare our formation estimates with several recent estimates also obtained using the Walin
 453 method. Badin and Williams (2010), using two different air-sea flux climatologies showed a
 454 transformation from dense to light water in the SAMW σ_θ range 26.8 - 27.2 kg/m³, whereas
 455 lighter waters ($25.0 < \sigma_\theta < 26.5$ kg/m³), outcropping farther equatorward, were transformed
 456 to denser waters by ocean heat loss. They estimated 16 Sv of formation of light water at
 457 $\sigma_\theta=26.6$ and 15 Sv of destruction of dense water at $\sigma_\theta=27.0$ emphasizing that the balance
 458 of freshwater and heat components differed in the three flux datasets.

459 Using a coarse resolution (2°x2°) global coupled ice-ocean model, Iudicone et al. (2008a)
 460 found that south of 50°S the heat flux is uniformly close to zero or slightly positive (ocean
 461 heating) and the buoyancy flux is dominated by freshening. Their associated Walin analysis
 462 yielded formation of 40 Sv in the broad σ_θ range of 26.0-27.2 kg/m³, of which 12 Sv were
 463 formed by ocean heat loss from thermocline water (with $\sigma_\theta < 26.0$ kg/m³), while 28 Sv of the
 464 denser varieties of mode water were formed by freshening of denser waters. For comparison,
 465 averaged over 2005-2006, SOSE formation of water in the σ_θ range 26.0-27.2 kg/m³ is 6.6 Sv,
 466 with 11.0 Sv formed by freshwater flux (almost entirely by freshening of denser water) and
 467 4.4 Sv destroyed by air-sea heat flux (almost entirely due to ocean heat loss, transforming
 468 more water out of than into the SAMW density range).

469 SOSE formation is thus weaker than Iudicone et al.'s (2008a) model-based result, and also
 470 weaker than Downes et al.'s (2011) results from the global 1° ECCO model and three free-
 471 running coupled climate models, which produced 26-51 Sv in the σ_θ range 26.0-27.2 kg/m³.
 472 The SOSE estimates of mode water formation are smaller because SOSE's adjusted surface

473 fluxes include much weaker ocean heat loss over the whole Southern Ocean and lower pre-
474 cipitation in the polar regions compared to the other widely used air-sea flux products, such
475 as NCEP1, ERA-Interim and LY09 (Cerovečki et al., 2011), resulting in smaller differential
476 cooling and freshwater gain over the outcrops bounding the wide SAMW density range con-
477 sidered in the other studies ($\sigma_\theta = 26.0$ and 27.2 kg/m³) (see also the Appendix). Although
478 the rates differ, the patterns of transformation in SOSE and in these other results are sim-
479 ilar, with water in the SEPSAMW and SEISAMW density ranges formed mainly through
480 buoyancy gain due to freshening and to a lesser extent heat gain, while lighter waters (with
481 $\sigma_\theta < 26.2$ kg/m³) were formed through heat loss and evaporation.

482 **4.6 Seasonal and geographic distributions of SAMW transforma-** 483 **tion and formation**

484 The seasonal cycle of buoyancy gain and loss for each global density outcrop is depicted
485 through monthly averages of the five-day averaged transformation rate estimates from Sec-
486 tion 4.1 (Figure 10). From April through September (austral winter), transformation rates
487 are positive (the ocean loses buoyancy), while from October through March (austral sum-
488 mer), transformation rates are negative (the ocean gains buoyancy), as expected. Transfor-
489 mations due to winter cooling and summer warming, whose magnitude reaches more than
490 200 Sv at the lower densities shown in Figure 10, nearly cancel, so that the annually averaged
491 transformation rates, of less than 10 Sv, are much smaller than the monthly mean rates.

492 Following Brambilla et al. (2008) and Maze et al. (2009), we next consider geographical
493 maps of transformation and formation for different seasons and the annual mean, which
494 provide more physical understanding of the water mass formation process. Figures 11 and
495 12 show that both the SEISAMW and SEPSAMW outcrop windows move poleward in
496 summer (October through March) and equatorward in winter (April through September),
497 as expected.

498 The strongest local transformation of water into the SEISAMW density range is due to
499 large ocean buoyancy loss during austral winter south of Australia and New Zealand as well
500 as in the central South Pacific (Figure 11c, e). Here more water is added at $\sigma_\theta=26.75 \text{ kg/m}^3$
501 than is removed at $\sigma_\theta=26.85 \text{ kg/m}^3$ (compare Figure 11c,d), resulting in SEISAMW for-
502 mation (Figure 13c,e). These SEISAMW formation regions coincide with the location of
503 deepest winter mixed layers (Dong et al., 2008) and the lowest PV pools in the SEISAMW
504 density range (Figures 4a-c).

505 The southeast Pacific is another region with strong winter transformation of water into
506 the SEISAMW density range by ocean buoyancy loss, which however removes more water out
507 of the SEISAMW density range (to become denser than $\sigma_\theta=26.85 \text{ kg/m}^3$) than adds by the
508 transformation of lighter water (with $\sigma_\theta < 26.75 \text{ kg/m}^3$) into the SEISAMW density range,
509 yielding net destruction of water in the SEISAMW density range in this region (Figure 13c).

510 In the SEPSAMW formation region off the coast of Chile, air-sea buoyancy (heat) loss
511 transforms more water into than out of the SEPSAMW density range (Figure 12c,d), yielding
512 SEPSAMW formation (Figure 13d,f). The SEPSAMW formation region coincides with the
513 location of deep winter mixed layers (Dong et al., 2008 contours shown on the maps).

514 The transformation and formation maps thus reveal information that the integrated
515 global Walin calculations obscure. For both SEPSAMW and SEISAMW, differential buoy-
516 ancy loss leads to formation of water in the region of the lowest PV SAMWs; the transfor-
517 mation maps show that at the SAMW formation sites in the southeast Indian and southeast
518 Pacific Ocean marked by lowest PV, these water masses are formed only from lighter water
519 by strong ocean buoyancy (heat) loss in austral winter. For SEPSAMW, conclusions from
520 the maps match the Pacific-wide Walin calculation, with the most developed (lowest PV)
521 SEPSAMW formed through buoyancy loss, even though the global Walin calculation yields
522 formation of SEPSAMW density class water through buoyancy gain. For SEISAMW, in
523 contrast, both the Indian-only and global Walin calculations show that SEISAMW density

524 class water is formed by differential buoyancy gain, dominated by freshwater gain, whereas
 525 the lowest PV pool is associated with buoyancy loss due to cooling.

526 **5 SAMW volume budget and diapycnal mixing forma-** 527 **tion estimate**

528 The formation/destruction rate associated with diapycnal mixing within the Southern Ocean
 529 south of 30°S is the difference between the storage (volume change) (Sections 5.2), and
 530 volume transport across 30°S (Section 5.1) and air-sea flux formation (Eq. (7)). We consider
 531 this budget not only for the Southern Ocean as a whole, but also in the Indian, Pacific and
 532 Atlantic sectors individually.

533 **5.1 Volume transport across 30°S and between ocean sectors**

534 Volume transport across the complete 30°S section (Figure 14a and Table 1) is divided
 535 into southward transport of upper thermocline water at densities lower than $\sigma_\theta=25.5$ kg/m³
 536 and net northward transport of 31.0 Sv of the subducted, denser underlying layer, with
 537 the maximum density considered here of 27.1 kg/m³ for reasons described in Section 2.2.3.
 538 This northward transport is distributed over all three ocean sectors. The globally-integrated
 539 northward transport peaks at $\sigma_\theta=26.6$ -26.8 kg/m³, due to northward transport of SEISAMW
 540 in the Indian Ocean, and remains high at the higher densities of SEPSAMW in the Pacific,
 541 and of AAIW in the Atlantic. In Talley (2003, 2008) (Table 1), the cross-over between
 542 southward and northward transport was at a higher density ($\sigma_\theta=26.4$ to 26.5 kg/m³) than
 543 in SOSE. SOSE's northward transport between $\sigma_\theta=25.5$ and 25.8 kg/m³ mostly lies in the
 544 Pacific, associated with the Subtropical Mode Water of the East Australian Current (Roem-
 545 mich and Cornuelle, 1992), and its northward transport between $\sigma_\theta=25.8$ and 26.6 kg/m³
 546 mostly lies in the Atlantic associated with the Subtropical Mode Water of the Brazil Current
 547 (Provost et al., 1999).

548 Focusing on SAMW transports in the σ_θ range 26.7-27.0 kg/m³, SOSE's northward trans-
 549 port is similar to Talley's (2003) in all ocean sectors. SOSE's transport in the Pacific (4.6 Sv)
 550 and Atlantic (4.4 Sv) sectors agree well with Talley's (2003) 2.2 Sv and 4.1 Sv, respectively
 551 (Table 1). In the Indian Ocean, both Talley (2003) and SOSE yield northward transport
 552 of 1.5 Sv in the lighter SEISAMW σ_θ range 26.7-26.89 kg/m³, and southward transport in
 553 the denser σ_θ range 26.89-27.0 kg/m³, lying between SEISAMW and AAIW (-1.5 Sv and
 554 -1.1 Sv, respectively).

555 Also, Iudicone et al.'s (2008a,c) estimates of northward transport across 30°S in the σ_θ
 556 range 26.0-27.2 kg/m³ (7.2, 2.7, and 9.5 Sv in the Pacific, Indian and Atlantic) are similar
 557 to the corresponding SOSE estimates of 7.9, 3.1, and 14.5 Sv, respectively (Table 1).

558 Between the ocean sectors, the eastward flow of SAMW ($\sigma_\theta = 26.7-27.1$ kg/m³) is the
 559 strongest from the Indian to the Pacific (43 Sv) (Figure 14 e-g; Table 2). It decreases to
 560 36 Sv from the Pacific to the Atlantic Ocean and further to 26 Sv from the Atlantic to the
 561 Indian. This pattern reflects the dominance of SAMW formation in the southeast Indian
 562 Ocean.

563 5.2 Storage rate in isopycnal layers

564 A non-zero storage rate (volume change) (Eq. (7)) is a consequence of the non-stationarity
 565 of this 2-year estimate. The rates of volume change each year were comparable to the for-
 566 mation, advective export, and destruction rates (Figure 14 h-k compared with the advective
 567 transports in panels a-g). Volume loss occurred at the SAMW and AAIW densities (σ_θ
 568 range 26.4-27.0 kg/m³), with compensating volume gain predominantly at higher densities
 569 (Figure 14h). Volume decrease was large in the Indian and Pacific, with a weak volume
 570 increase in the Atlantic (Table 2). Maps of volume loss (not shown) show that the loss tends
 571 to be localized in the regions of lowest PV SAMW. Details of storage rates are provided in
 572 the next section as they are required for calculation of the diapycnal mixing rate.

573 5.3 SAMW formation/destruction budgets south of 30°S

574 We show here that water mass formation/destruction due to diapycnal diffusive fluxes (D
 575 term in Eq. (2)) are comparable in magnitude to the air-sea flux formation rate, export
 576 transports, and storage rates; all contribute to the SAMW budget. Elevated diapycnal
 577 mixing is expected close to the sea surface, within and in the proximity of the mixed layer
 578 where diffusivities are enhanced (Marshall et al., 1999; Iudicone et al., 2008b).

579 We first consider the broad σ_θ range 26.5-27.1 kg/m³, which includes all varieties of
 580 SAMW discussed in Section 4, both in terms of the global (circumpolar) outcrops and in
 581 each ocean sector (Tables 3 and 4; Figure 15). We then highlight narrow density ranges of
 582 the SEISAMW, SEPSAMW, and the weaker South Atlantic SAMW (Table 4).

583 *a) Southern Ocean as a whole.* Considering the global SAMW budget south of
 584 30°S, net formation in the density range 26.5 – 27.1 kg/m³ was (13.2, 6.8) Sv for (2005,
 585 2006) (Table 2a). The northward transport across 30°S was (18.2, 17.1) Sv and the volume
 586 decreased at a rate of (-19.3, -22.9) Sv. Therefore approximately (14.5, 12.6) Sv of SAMW
 587 was removed by diapycnal mixing (Figure 15a) in the Indian and Pacific Oceans.

588 In the narrower density range ($\sigma_\theta = 26.7$ -27.1 kg/m³) the balance is similar. Air-sea
 589 buoyancy fluxes formed (13.5, 1.9) Sv (Table 2b). Combined with the northward transport
 590 of (13.4, 12.6) Sv across 30°S, and a storage rate of (-7.8, -23.3) Sv, diapycnal mixing removed
 591 SAMW at a rate of (8.0, 12.6) Sv in the Indian and Pacific Oceans.

592 Thus, air-sea fluxes and diapycnal mixing play equally important roles in the SAMW
 593 budget. We might conclude that the overall SAMW budget of formation and destruction is
 594 nearly closed south of 30°S. However, since the northward transport of SAMW out of the
 595 Southern Ocean and the rate of volume loss are similarly large, it is difficult to speculate
 596 about which terms would balance in a long-term climatological mean for which the storage
 597 rate should be negligible.

598 ***b) Indian Ocean.***

599 In the Indian Ocean, SAMW in the broad σ_θ range 26.5-27.1 kg/m³ is formed predomi-
 600 nantly by buoyancy gain from denser water (9.4, 10.9 Sv). Advection imports (29.8, 27.9) Sv
 601 from the Atlantic, exports (45.3, 45.1) Sv eastward to the Pacific (Table 2a; Figure 14e,g),
 602 and exports a much smaller (3.6, 2.9) Sv northward across 30°S. Thus overall, transports out
 603 of the Indian Ocean exceed import by (19.1, 20.4) Sv, which can be associated with the large
 604 SEISAMW formation compared with SEPSAMW and South Atlantic SAMW formation.
 605 Taken together with formation of (9.4, 10.9) Sv by air-sea fluxes, and a storage rate (volume
 606 loss) of (-16.3, -12.3) Sv, we estimate that diapycnal mixing removes (-6.6, -3.1) Sv (Table
 607 2a, Figure 15a). Thus a large amount of Indian SAMW is formed through air-sea fluxes,
 608 and almost half of this volume is destroyed in Indian Ocean through diapycnal mixing.

609 In the narrower σ_θ range (26.7-27.1 kg/m³), there is net formation by air-sea buoyancy
 610 fluxes (8.5, 6.3 Sv), net export of (15.6, 17.8) Sv mostly eastward to the Pacific, and volume
 611 loss of (-7.3, -11.5) Sv, from which we diagnose weak formation by diapycnal mixing (1.3,
 612 1.0 Sv) (Table 2b).

613 In the narrowest density range 26.75-26.85 σ_θ , associated with the lowest PV SEISAMW,
 614 there is a net formation by air-sea buoyancy fluxes (7.1, 7.8 Sv), and destruction by diapycnal
 615 mixing (-5.5, -1.0 Sv; Table 3). Zonal export to the Pacific (13.0, 12.7 Sv) in this SEISAW
 616 range remains much stronger than import from the Atlantic (3.7, 2.7 Sv).

617 Largely consistent with the results presented here, Sloyan and Rintoul (2001b) used a
 618 static inverse box model to infer that the largest SAMW formation is in the Indian sector of
 619 the Southern Ocean, where formation in the σ_θ range 26.0-27.0 kg/m³ is from both lighter
 620 and denser water: 4.4 ± 2.0 Sv of thermocline water transforms into SAMW, joined by
 621 11.7 ± 1.0 Sv of Antarctic Surface Water which is advected northward in the Ekman layer,
 622 warmed, freshened and transformed to SAMW densities, for a net formation of 16.1 Sv
 623 by air-sea fluxes. They estimate 4 ± 2 Sv of SAMW destruction by diapycnal mixing as

624 it is converted to denser water. (In SOSE, averaged over two years in the σ_θ range 26.0-
 625 27.0 kg/m³, 6.8 Sv are formed by air-sea fluxes, 3.5 Sv are exported northward, 37.5 Sv
 626 are transported into the Pacific, and 21.9 Sv are transported from the Atlantic. Since the
 627 storage rate was -8.9 Sv, diapycnal mixing is inferred to have formed 3.4 Sv.)

628 ***c) Pacific Ocean.***

629 In the Pacific in the $\sigma_\theta = 26.5\text{-}27.1$ kg/m³ range, air-sea fluxes destroyed (-1.1, -4.6) Sv.
 630 This was not large enough to balance the small net advective inflow of (1.7, 1.0) Sv, and the
 631 volume decrease at (-5.0, -12.0) Sv. Therefore diapycnal mixing rate is estimated to have
 632 removed (-5.6, -8.4) Sv in this density range.

633 In the somewhat narrower density range ($\sigma_\theta = 26.7\text{-}27.1$ kg/m³), the budget is qual-
 634 itatively similar: (42.8, 42.8) Sv was transported into the Pacific from the Indian, (35.5,
 635 35.9) Sv was transported out to the Atlantic, and (6.0, 5.5) Sv was transported northward,
 636 yielding a near balance of (1.3, 1.4) Sv inflow in the Pacific. SAMW in this range can be
 637 either formed or destroyed by air-sea buoyancy fluxes: (2.2, -1.0 Sv). The volume loss rate
 638 was (-5.4, -13.2) Sv, implying that (-8.9, -13.6) Sv was destroyed by diapycnal mixing (Table
 639 2b).

640 Looking at the narrowest density range ($26.95 < \sigma_\theta < 27.05$ kg/m³), which is characteris-
 641 tic of SEPSAMW (Table 3), air-sea buoyancy fluxes formed (5.6, 4.1) Sv. This is unlike the
 642 net destruction or weak formation obtained for the wider density ranges that included the
 643 inflowing SEISAMW which is partially destroyed in the Pacific through air-sea fluxes (likely
 644 through conversion to SEPSAMW). Net advective export was (-6.4, -5.5) Sv, and the volume
 645 decrease was (-2.6, -4.8) Sv. The diagnosed diapycnal nearly zero formation or destruction
 646 is therefore (0.5, -1.2) Sv.

647 As in SOSE, Sloyan and Rintoul (2001b) inferred strong destruction in the broad σ_θ
 648 range 26.0-27.0 kg/m³ by diapycnal mixing in the Pacific: 8 Sv of cold and fresh SAMW
 649 was transformed to thermocline water by a combined effect of air-sea buoyancy fluxes and

650 diapycnal fluxes, and 10.4 ± 2.0 Sv of SAMW was transformed into denser water (AAIW
 651 and Upper Circumpolar Deep Water) by diapycnal mixing. Some of 3.3 ± 1 Sv of SAMW
 652 formed from Antarctic Surface Water is further converted to slightly denser AAIW. (For
 653 comparison, in SOSE, averaged over two years in the σ_θ range 26.0-27.0 kg/m³, 1.6 Sv were
 654 destroyed by air-sea fluxes, 6.7 Sv were exported northward, 37.5 Sv were transported into
 655 the Pacific, and 26.7 Sv were transported out of the Pacific into the Atlantic . The storage
 656 rate was -10.3 Sv, and therefore diapycnal mixing destroyed 12.8 Sv.)

657 *d) Atlantic Ocean.*

658 The South Atlantic SAMW is much weaker than the Indian and Pacific SAMWs in terms
 659 of its PV signal (Figure 3), and it has only a weak formation peak in the global surface
 660 formation rates (Figure 8). In the broad SAMW density range ($\sigma_\theta=26.5$ -27.1 kg/m³) there
 661 is import from the Pacific (37.0, 38.0 Sv), and export both northward across 30°S (7.9,
 662 8.1 Sv) and eastward into the Indian Ocean (29.8, 27.9 Sv), hence a net gain of (0.7, 2.0) Sv
 663 by advective transports within the Atlantic (Table 2a). Air-sea fluxes form SAMW in the
 664 South Atlantic from denser waters at a rate of (5.0, 0.5) Sv and since the volume of SAMW
 665 in the South Atlantic has increased by (2.0, 1.4) Sv, a net destruction of (-2.3, -1.1) Sv of
 666 SAMW is ascribed to diapycnal mixing.

667 In the narrower density range ($\sigma_\theta = 26.7$ -27.1 kg/m³), air-sea fluxes yielded either for-
 668 mation or destruction (2.8, -3.4 Sv). There was net advection into the region (2.4, 4.8 Sv)
 669 despite the robust northward transport out of the region, because of the large Drake Passage
 670 transport of SEPSAMW. There was a net addition to the volume in the SAMW layer (4.8,
 671 1.4 Sv). The balance for diapycnal mixing is close to zero (-0.4, 0.0 Sv).

672 For the narrowest density range characteristic of South Atlantic SAMW ($26.55 < \sigma_\theta <$
 673 26.65 kg/m³) (Table 3), (1.8, 2.9) Sv was formed by air-sea buoyancy fluxes. For this
 674 narrowest density range of Atlantic SAMW, there is a net export of (-1.7, -1.2) Sv unlike the
 675 net inflow for the wider density range which includes the large import of SEPSAMW from

676 the Pacific. Including the similar magnitude volume change of (-1.0, 0.3) Sv, we diagnose
677 (-1.1, -1.4) Sv destroyed by diapycnal mixing.

678 Sloyan and Rintoul (2001b), for $\sigma_\theta = 26.0\text{-}27.0$ kg/m³, showed a cancelation between
679 surface and interior SAMW transformation in the Atlantic Ocean, with air-sea buoyancy
680 fluxes transforming 6.0 ± 1.0 Sv of thermocline water into SAMW, which is more than
681 compensated by diapycnal mixing converting 8.0 ± 3.0 Sv of SAMW back into thermocline
682 water.

683 **6 Discussion and Conclusions**

684 The Southern Ocean (south of 30°S) is characterized by globally important water mass trans-
685 formations, including those that govern the upper ocean's SAMWs (e.g. Speer et al., 2000;
686 Sloyan and Rintoul, 2001a,b; Talley et al., 2003; Talley, 2008). Formation and destruction
687 rates by air-sea fluxes and by diapycnal mixing, as well as transports and storage, of wa-
688 ters in the SAMW density range were estimated using the Southern Ocean State Estimate
689 (SOSE) (Mazloff et al., 2010), which has eddy-permitting resolution and which is constrained
690 to a large set of oceanic observations. Importantly for water mass formation analysis, SOSE
691 provides both three-dimensional oceanic fields and adjusted air-sea fluxes that are dynam-
692 ically consistent so that they exactly satisfy the ocean circulation model equations, which
693 is central to water mass formation analysis. SAMW surface formation rates were calculated
694 using Walin (1982) analysis with SOSE air-sea fluxes and surface densities for 2005 and 2006.
695 Meridional transport of SAMW out of the Southern Ocean across 30°S, zonal transport be-
696 tween the ocean basins, and the rate of volume change for each year were calculated. The
697 SAMW formation/destruction rate due to diapycnal mixing was estimated as the residual of
698 these other rates (Eq. 7). An important result is that all rates (air-sea fluxes, net advection,
699 storage, diapycnal mixing) are of similar magnitude, so none can be neglected or considered

700 to balance a single other rate.

701 Considering the entire Southern Ocean south of 30°S in the density range $26.5 < \sigma_\theta <$
702 27.1 kg/m^3 , which includes SAMW, there was formation by air-sea fluxes (13.2, 6.8 Sv) for
703 (2005, 2006) and destruction by diapycnal mixing (-14.5, -12.6 Sv). (Qualitatively similar
704 results were obtained for a slightly narrower density range.) There was a net northward
705 export out of the Southern Ocean of (18.2, 17.1) Sv (distributed over all three ocean basins)
706 and a significant loss of volume at a rate of (-19.3, -22.9) Sv over the two years of the SOSE
707 output. One interpretation could be that the Southern Ocean south of 30°S is a sufficiently
708 large region that the water in the SAMW density range is nearly self-contained, with most of
709 the water formed through air-sea fluxes subsequently destroyed through diapycnal mixing, as
710 concluded by Marshall et al. (1999) for a large region of the North Atlantic; the northward
711 export would then nearly balance the net volume loss. An alternative interpretation is
712 that water in the SAMW density range formed through air-sea fluxes is mostly transported
713 northward out of the Southern Ocean, while regional diapycnal mixing creates the net volume
714 loss for these two years. In other words, the volume decrease is so large over the two years that
715 it is difficult to anticipate the relative reduction in northward export versus the diagnosed
716 diapycnal flux if enough years were available to produce a more stationary average.

717 Zonal advective exchanges between the ocean basins follow the pattern of dominant
718 SAMWs: the highest eastward transport is from the Indian to the Pacific, associated with
719 strong SEISAMW production in the Indian, the second highest is from the Pacific to the At-
720 lantic, incorporating the strong SEPSAMW production at a higher density than SEISAMW,
721 and the weakest is from the Atlantic to the Indian. Each ocean basin has net merid-
722 ional/zonal advective export in its own narrow SAMW density range, even though over
723 the entire density range considered, only the Indian Ocean has a net export. Water formed
724 in the Indian Ocean in the broad SAMW density range that is transported to Pacific is
725 destroyed there both by air-sea buoyancy fluxes (-1.1, -4.6) Sv and diapycnal mixing (-5.6,

726 -8.4) Sv.

727 Air-sea flux formation rates peak at the SEISAMW and SEPSAMW densities: these are
728 also the dominant SAMWs in terms of low PV on isopycnals. Formation is due equally to
729 heat and freshwater processes. In the SEISAMW and SEPSAMW density ranges integrated
730 globally over the Southern Ocean, SEISAMW ($26.75 < \sigma_\theta < 26.85 \text{ kg/m}^3$) is formed from both
731 lighter water (by air-sea heat loss) and denser water (by air-sea heat gain and freshening).
732 Water in the SEPSAMW density range ($26.95 < \sigma_\theta < 27.05 \text{ kg/m}^3$) is formed globally from
733 denser water (by freshening) and considerably less from lighter water (by air-sea heat loss).
734 However, within the regions of their strongest mode water signatures, that is the lowest PV
735 on isopycnals and deepest winter mixed layers, both SEISAMW and SEPSAMW are formed
736 from lighter water through buoyancy (heat) loss.

737 The enhanced volume loss over these two years in the SEISAMW and SEPSAMW low
738 PV pools suggests that formation in these regions was not as vigorous in these two years as
739 over the longer term. The Southern Annular Mode index reached a relative decadal low in
740 2005 and 2006, compared with a high achieved in the late 1990s; a high Southern Annular
741 Mode index has been shown to coincide with increased Southern Hemisphere subtropical
742 gyre circulation, which carries SEISAMW and SEPSAMW more rapidly into the subtropical
743 gyres (McDonagh et al., 2005; Roemmich et al., 2009). Therefore, until a longer time
744 series is available, we cannot draw conclusions about the relative quantitative importance
745 for subtropical ventilation of waters formed from less dense upper ocean water (i.e. low PV
746 SAMW itself) compared with waters arising from the very long circumpolar outcropping
747 regions in which there is little mode water formation, and where water mass formation is
748 dominated by upwelling of denser water which gains buoyancy from air-sea fluxes.

749 *Acknowledgements* This work was supported by NSF Ocean Sciences grants OCE-0327544
750 and OCE-0850869 to Scripps Institution of Oceanography. NCEP Reanalysis data are pro-
751 vided by the NOAA/OAR/ESRL PSD, Boulder, Colorado, USA, from their web site at
752 <http://www.cdc.noaa.gov/>.

753 The ERA-Interim, GODAS and LY09 (LY09 is listed as “Coare2.0 Global air-sea flux
754 dataset” data used in this study are from the Research Data Archive (RDA) which is
755 maintained by the Computational and Information Systems Laboratory (CISL) at the Na-
756 tional Center for Atmospheric Research (NCAR). NCAR is sponsored by the National
757 Science Foundation (NSF). The original ERA-Interim data are available from the RDA
758 (<http://dss.ucar.edu>) in dataset number ds627.0. The original LY09 data used here are
759 available from the RDA (<http://dss.ucar.edu>) in dataset number ds260.2. The GODAS data
760 are available from the RDA (<http://dss.ucar.edu>) in dataset number ds277.6. We thank
761 Sarah Gille and Janet Sprintall for motivating discussions.

762 **Appendix: Walin SAMW surface formation rates using** 763 **other air-sea buoyancy flux products**

764 How sensitive are the SOSE Walin formation rate estimates to the specific air-sea flux data
765 set that is used, given that commonly-used flux products differ so much in the poorly sampled
766 Southern Ocean? In Cerovečki et al. (2011) we compared the SOSE air-sea buoyancy fluxes
767 with NCEP1, the ERA-Interim reanalysis by ECMWF, and LY09. Here we calculate SAMW
768 formation rates from each of these products, and also from the OCCA state estimate that
769 is used to constrain the initial and northern boundary conditions in SOSE (Figure A1).

770 SOSE and OCCA provide all of the variables needed to estimate the air-sea buoyancy
771 flux, but sea surface salinity (SSS) must be obtained externally for the freshwater fluxes for
772 NCEP1, ERA, and LY09. For NCEP1 and ERA we used SSS from the NCEP Global Ocean
773 Data Assimilation System (GODAS) (Behringer and Xue, 2004). For LY09, we used SSS
774 from the Polar Science Center Hydrographic Climatology (PHC2), which is a blending of the
775 Levitus et al. (1998) and Steele et al. (2001) datasets, following Danabasoglu et al. (2009)
776 and Griffies (personal communication). SST for LY09 was also required and was taken from
777 the Hadley Centre sea surface temperature (Rayner et al., 2003).

778 We focus on the formation peaks that occur in the SEISAMW and SEPSAMW density
779 ranges (Figure A1; Table A1). The SEISAMW formation rate estimates obtained from the
780 various products differ less than those of SEPSAMW. Overall, averaged over all five products
781 and both years, the SEISAMW formation rate was (7.3, 8.2) Sv and SEPSAMW formation
782 was (5.2, 4.0) Sv. SOSE taken by itself, averaged over both years, yields (5.8, 8.0) Sv of
783 SEISAMW and (6.3, 3.2) Sv of SEPSAMW, clearly within the range of the whole group of
784 products.

785 SOSE yields two distinct peaks in water mass formation at the SEISAMW and SEP-
786 SAMW densities that are inferred from the low PV distribution (Section 3 and histori-

787 cally). LY09 also yields two distinct formation peaks for SEISAMW and SEPSAMW, but
788 the SEISAMW peak is at somewhat lower density ($\sigma_\theta = 26.7 \text{ kg/m}^3$) than the observed mode
789 water. Formation rate estimates obtained from the other air-sea buoyancy flux products yield
790 a wide peak in water mass formation spanning the whole SAMW density range, with no dif-
791 ferentiation between SEISAMW and SEPSAMW (Figure A1), which is unphysically coarse
792 given the clearly separate SEISAMW and SEPSAMW signals in PV.

References

- 793
- 794 Badin, G., and R. G. Williams, 2010: On the buoyancy forcing and residual circulation in
795 the Southern Ocean: the feedback from Ekman and eddy transfer. *J. Phys. Oceanogr.*, **40**,
796 295-310. doi: 10.1175/2009JPO4080.1.
- 797
- 798 Brambilla, E., L. D. Talley, and P. E. Robbins, 2008: Subpolar mode water in the northeast-
799 ern Atlantic: 2. Origin and transformation. *J. Geophys. Res.*, **113**, C04026. doi:10.1029/
800 2006JC004063.
- 801
- 802 Behringer D.W., and Y. Xue, 2004: Evaluation of the global ocean data assimilation system
803 at NCEP: The Pacific Ocean. Eighth Symposium on Integrated Observing and Assimilation
804 Systems for Atmosphere, Oceans, and Land Surface, AMS 84th Annual Meeting, Washing-
805 ton State Convention and Trade Center, Seattle, Washington, 11-15.
- 806
- 807 Bourassa, M.A., S.T. Gille, C. Bitz, D. Carlson, I. Cerovecki, C.A. Clayson, M. F. Cronin,
808 W.M. Drennan, C. W. Fairall, R. Hoffman, G. Magnusdottir, R. T. Pinker, I. A. Renfrew,
809 M. Serreze, K. Speer, L. Talley, G. A. Wick, 2012: High-Latitude Ocean and Sea-Ice Surface
810 Fluxes: Challenges for Climate Research. *Bull. Amer. Met. Soc.*, submitted.
- 811
- 812 Cerovečki, I., L. Talley, and M. Mazloff, 2011: Southern Ocean air-sea buoyancy flux esti-
813 mates. *J. Clim.*, **24**, 6283-6306.
- 814
- 815 Cerovečki, I., J. Marshall, 2008: Eddy modulation of air-sea interaction and convection. *J.*
816 *Phys. Oceanogr.*, **38**, 65-83.

817

818 Danabasoglu G., S., Peacock, K. Lindsay, and D. Tsumune, 2009: Sensitivity of CFC-11
819 uptake to physical initial conditions and interannually varying surface forcing in a global
820 ocean model. *Ocean Modell.*, **29**, 58-65.

821

822 da Silva, A. M., C. C. Young, and S. Levitus, 1995a: Anomalies of Heat and Momentum
823 Fluxes. Vol. 3, Atlas of Surface Marine Data 1994, NOAA Atlas NESDIS 8, 413 pp.

824

825 da Silva, A. M., C. C. Young, and S. Levitus, 1995b: Anomalies of Fresh Water Fluxes. Vol.
826 4, Atlas of Surface Marine Data 1994, NOAA Atlas NESDIS 9, 308 pp.

827

828 Dong, S, J. Sprintall, S. Gille, and L. Talley, 2008. Southern Ocean mixed-layer depth from
829 Argo float profiles. *J. Geophys. Res.*, **113**, C06013, doi:10.1029/2006JC004051.

830

831 Downes, S. M., A. Gnanadesikan, S. M. Griffies, and J. L. Sarmiento, 2011: Water mass ex-
832 change in the Southern Ocean in coupled climate models. *J. Phys. Oceanogr*, **41**, 1756-1771.

833

834 Fine, R.A., 1993: Circulation of Antarctic Intermediate Water in the Indian Ocean. *Deep-*
835 *Sea Research*, **40**, 2021-2042.

836

837 Forget, G., 2010: Mapping ocean observations in a dynamical framework: a 2004-2006 ocean
838 atlas. *J. Phys. Oceanogr*, **40**, 1201-1221, doi:10.1175/2011JPO4586.1.

839

840 Garrett, C., K. Speer, and E. Tragou, 1995: The relationship between water mass forma-
841 tion and the surface buoyancy flux, with application to Phillips' Red Sea model. *J. Phys.*
842 *Oceanogr.*, **25**, 1696-1705.

843

844 Gill, A. E., 1982: *Atmosphere-Ocean Dynamics*. Academic Press, New York, 662 pp.

845

846 Grist, J. P. and S. A. Josey, 2003: Inverse analysis adjustment of the SOC airsea flux clima-
847 tology using ocean heat transport constraints. *J. Clim.*, **16**, 3274-3295.

848

849 Hallberg, R., and A. Gnanadesikan, 2006: The role of eddies in determining the structure
850 and response of the wind-driven Southern Hemisphere overturning: Results from the Mod-
851 eling Eddies in the Southern Ocean (MESO) project. *J. Phys. Oceanogr.*, **36**, 2232-2252.

852

853 Hanawa, K. and L. D. Talley, 2001: Mode Waters. In: Siedler, G., Church, J., Gould, J.
854 (Eds.), *Ocean circulation and climate*. International Geophysics Series, Vol. 77. Academic
855 Press, New York, 373-386.

856

857 Hartin, C.A., R. A. Fine, B. M. Sloyan, L. D. Talley, T. K. Chereskin, and J. Happell, 2011:
858 Formation rates of Subantarctic Mode Water and Antarctic Intermediate Water within the
859 South Pacific. *Deep-Sea Res. I*, **58**, 524-534.

860

861 Heywood, K. J., A. C. Naveira Garabato and D. P. Stevens, 2002: High mixing rates in the
862 abyssal Southern Ocean. *Nature*, **415**, 1011-1014.

863

864 Holte, J.W., 2010: Subantarctic Mode Water formation: air-sea fluxes and cross-frontal ex-
865 change. PhD dissertation, University of California San Diego, 112 pp.

866

867 Holte, J.W., L. D. Talley, T.K. Chereskin, and B. M. Sloyan, 2012: The role of air-sea fluxes
868 in Subantarctic Mode Water formation. *J. Geophys. Res.*, **117**, C03040, doi:10.1029/2011JC007798

869 .

870

871 Holte, J.W., L. D. Talley, T.K. Chereskin, and B. M. Sloyan, in preparation: Exchange across
872 the Subantarctic Front and Subantarctic Mode Water formation in the southeast Pacific. *J.*
873 *Geophys. Res.*, in preparation.

874 Ito, T., M. Woloszyn, and M. Mazloff, 2010: Anthropogenic carbon dioxide transport in the
875 Southern Ocean driven by Ekman flow. *Nature*, **463**, 80-83.

876

877 Iudicone, D., G. Madec, B. Blanke, and S. Speich, 2008a: The role of Southern Ocean surface
878 forcings and mixing in the global conveyor. *J. Phys. Oceanogr.*, **38**, 1377-1400.

879

880 Iudicone, D., G. Madec, and T. J. McDougall, 2008b: Water-Mass transformations in a
881 neutral density framework and the key role of light penetration. *J. Phys. Oceanogr.*, **38**,
882 1357-1376.

883

884 Iudicone, D., S. Speich, G. Madec, and B. Blanke, 2008c: The global conveyor belt from a
885 Southern Ocean perspective. *J. Phys. Oceanogr.*, **38**, 1401-1425.

886

887 Josey, S. A., E. C. Kent, and P. K. Taylor, 1998: The Southampton Oceanography Centre
888 (SOC) ocean-atmosphere heat, momentum and freshwater flux atlas. Southampton Oceanog-
889 raphy Centre Rep., **6**, 30 pp.

890

891 Kalnay, E., M. Kanamitsu, R. Kistler, W. Collins, D. Deaven, L. Gandin, M. Iredell, S.
892 Saha, G. White, J. Woolen, Y. Zhu, M. Cheliah, W. Ebisuzaki, W. Higgins, J. Janowiak, J.,
893 K.C. Mo, C. Ropelewski, A. Leetmaa, R. Reynolds, and R. Jenne, 1996: The NCEP/NCAR
894 reanalysis project. *Bull. Am. Meteor. Soc.*, **77**, 437-471.

895

896 Karsten, R., and J. Marshall, 2002: Constructing the residual circulation of the Antarctic
897 Circumpolar Current from observations. *J. Phys. Oceanogr.*, **32**, 3315-3327.

898

899 Karstensen, J., and D. Quadfasel, 2002: Formation of Southern Hemisphere thermocline
900 waters: water mass conversion and subduction, *J. Phys. Oceanogr.*, **32**, 3020-3038.

901

902 Large, W. G., and A. J. G. Nurser, 2001: Ocean surface water mass transformation. In:
903 Siedler, G., Church, J., Gould, J. (Eds.), *Ocean Circulation and Climate*. International
904 Geophysics Series, Vol. 77. Academic Press, New York, 317-336.

905

906 Large, W., and S. Pond, 1981: Open ocean momentum flux measurements in moderate to
907 strong winds. *J. Phys. Oceanogr.*, **11**, 324-336.

908

909 Large, W. G. and S.G. Yeager, 2009: The global climatology of an interannually varying
910 air-sea flux data set. *Clim. Dyn.*, **33**, 341-364.

911

912 Levitus, S., T. P. Boyer, M. E. Conkright, T. O'Brien, J. Antonov, C. Stephens, L. Statho-
913 plos, D. Johnson, and R. Gelfeld, 1998: Introduction. Vol. 1, World Ocean Database 1998.
914 NOAA Atlas NESDIS 18, *U.S. Gov. Printing Office, Wash., D.C.*, 346 pp.

915

916 Macdonald, A. M., and C. Wunsch, 1996: An estimate of global ocean circulation and heat
917 fluxes. *Nature*, **382**, 436-439.

918

919 Marshall, J., D. Jamous, and J. Nilsson, 1999: Reconciling thermodynamic and dynamic
920 methods of computation of water-mass transformation rates. *Deep-Sea Res.*, **46**, 545-572.

921

922 Maze, G., G. Forget, M. Buckley, J. Marshall, and I. Cerovečki, 2009: Using transformation
923 and formation maps to study the role of air-sea heat fluxes in North Atlantic eighteen degree
924 water formation. *J. Phys. Oceanogr.*, **39**, 1818-1835.

925

926 Mazloff, M., 2008: The Southern Ocean meridional overturning circulation as diagnosed
927 from an eddy permitting state estimate. *Ph.D. thesis, Massachusetts Institute of Technology*
928 *and the Woods Hole Oceanographic Institution, Cambridge, MA.*

929

930 Mazloff, M. R., P. Heimbach, and C. Wunsch, 2010: An eddy permitting Southern Ocean
931 state estimate. *J. Phys. Oceanogr.*, **40**, 880-899.

932

933 McCartney, M. S., 1977: Subantarctic Mode Water. In: A Voyage of Discovery: George
934 Deacon 70th Anniversary Volume, M. V. Angel, editor, Supplement to *Deep-Sea Res.*, Perg-
935 amon Press, Oxford, 103-119.

936

937 McCartney, M.S., 1982: The subtropical recirculation of Mode Waters. *J. Mar. Res.*, Sup-
938 plement to **40**, 427-464.

939

940 McCarthy, M. C. and L. D. Talley, 1999: Three-dimensional potential vorticity structure in
941 the Indian Ocean. *J. Geophys. Res.*, **104**, 13251-13267.

942

943 McDonagh, E.L., H. L. Bryden, B. A. King, R. J. Sanders, S. A. Cunningham, and R. Marsh,
944 2005: Decadal changes in the South Indian Ocean thermocline. *J. Clim.*, **18**, 1575-1590.

945

946 Molinelli, E.T., 1981: The Antarctic influence on Antarctic Intermediate Water. *J. Mar.*
947 *Res.*, **39**, 267-293.

948

949 Moore, G. W. K., and I. A. Renfrew, 2002: An assessment of the surface turbulent heat
950 fluxes from the NCEP reanalysis over western boundary currents. *J. Clim.*, **15**, 2020-2037.

951

952 Naveira Garabato, A. C., K. L. Polzin, B. A. King,, K. J. Heywood and M. Visbeck, 2004:
953 Widespread intense turbulent mixing in the Southern Ocean. *Science*, **303**, 210- 213.

954

955 Naveira Garabato, A. C., D. P. Stevens, and K. J. Heywood, 2003: Water mass conversion,
956 fluxes, and mixing in the Scotia Sea diagnosed by an inverse model. *J. Phys. Oceanogr.*, **33**,
957 2565-2587.

958

959 Naveira Garabato, A. C., D. P. Stevens, A. J. Watson and W. Roether, 2007: Short- cir-
960 cuiting of the overturning circulation in the Antarctic Circumpolar Current. *Nature*, **447**,
961 194-197.

962

963 Nurser, A. J. G., R. Marsh, and R. G. Williams, 1999: Diagnosing water mass formation
964 from air - sea fluxes and surface mixing. *J. Phys. Oceanogr.*, **29**, 1468-1487.

965

966 Piola, A. R., and D. T. Georgi, 1982: Circumpolar properties of Antarctic intermediate wa-
967 ter and Subantarctic Mode Water. *Deep Sea Research Part A*, **29**, 687-711.

968

969 Provost, C., C. Escoffier, K. Maamaatuaiahutapu, A. Kartavtseff, and V. Garcon, 1999:
970 Subtropical mode waters in the South Atlantic Ocean. *J. Geophys. Res.*, **104**, 21033-21049.

971

972 Rayner, N. A., D.E. Parker, E. B. Horton, C. K. Folland, L. V. Alexander, D. P. Rowell,
973 E. C. Kent, and A. Kaplan, 2003: Global analyses of sea surface temperature, sea ice, and

974 night marine air temperature since the late nineteenth century. *J. Geophys. Res.*, **108**, No.
975 D14, 4407 10.1029/2002JD002670.

976

977 Reid, J. L., 1994: On the total geostrophic circulation of the North Atlantic Ocean: Flow
978 patterns, tracers and transports. *Progress in Oceanography*, **33**, 1-92.

979

980 Reid, J. L., 1997: On the total geostrophic circulation of the Pacific Ocean: Flow patterns,
981 tracers and transports. *Progress in Oceanography*, **39**, 263-352.

982

983 Reid, J. L., 2003: On the total geostrophic circulation of the Indian Ocean: Flow patterns,
984 tracers and transports. *Progress in Oceanography*, **56**, 137-186.

985

986 Rintoul, S. R., 1991: South Atlantic interbasin exchange. *J. Geophys. Res.*, **96**, 2675-2692.

987

988 Rintoul, S., C. Hughes, and D. Olbers, 2001: The Antarctic Circumpolar Current System.
989 In: Siedler, G., Church, J., Gould, J. (Eds.), *Ocean circulation and climate*. International
990 Geophysics Series, Vol. 77. Academic Press, New York, 271-302.

991

992 Roemmich, D., J. Gilson, R. Davis, P. Sutton, S. Wijffels, and S. Rintoul, 2009: Decadal
993 spinup of the South Pacific subtropical gyre. *J. Phys. Oceanogr.*, **37**, 162-173.

994

995 Sabine, C. L., R. A. Feely, N. Gruber, R. M. Key, K. Lee, J. L. Bullister, R. Wanninkhof,
996 C. S. Wong, D. W. R. Wallace, B. Tilbrook, F. J. Millero, T.-H. Peng, A. Kozyr, T. Ono,
997 and A. F. Rios, 2004: The oceanic sink for anthropogenic CO₂. *Science*, **305**, 367-371.

998

999 Sallee, J. B., K. Speer, S. Rintoul and S. Wijffels, 2010: Southern Ocean thermocline venti-

1000 lation. *J. Phys. Oceanogr.*, **40**, 509-529.

1001

1002 Schmitz, W. J., 1996a: On the World Ocean circulation. Vol. II: The Pacific and Indian
1003 Oceans - A global update. Woods Hole Oceanogr. Inst. Tech. Rep. WHOI-96-08, 241 pp.

1004

1005 Sloyan, B.M., and I.V. Kamenkovich, 2007: Simulation of Subantarctic Mode and Antarctic
1006 Intermediate Waters in climate models. *J. Clim.*, **20**, 5061-5080.

1007

1008 Sloyan, B. M., and S. R. Rintoul, 2001a: The Southern Ocean limb of the global deep over-
1009 turning circulation. *J. Phys. Oceanogr.*, **31**, 143-173.

1010

1011 Sloyan, B. M., and S. R. Rintoul, 2001b: Circulation, renewal and modification of Antarctic
1012 mode and intermediate water. *J. Phys. Oceanogr.*, **31**, 1005-1030.

1013

1014 Sloyan, B., L. D. Talley, T. Chereskin, R. Fine and J. Holte, 2010: Antarctic Intermediate
1015 water and Subantarctic Mode water formation in the southeast Pacific: the role of turbulent
1016 mixing. *J. Phys. Oceanogr.*, **40**, 1558-1574.

1017

1018 Speer, K. G., H.-J. Isemer, and A. Biastoch, 1995: Global water mass formation from revised
1019 COADS data. *J. Phys. Oceanogr.*, **25**, 2444-2457.

1020

1021 Speer, K., Rintoul, S., and B. Sloyan, 2000: The diabatic Deacon cell. *J. of Phys. Oceanogr.*,
1022 **30**, 3212-3222.

1023

1024 Speer, K., and E. Tziperman, 1992: Rates of water mass formation in the North Atlantic
1025 Ocean. *J. Phys. Oceanogr.*, **22**, 93-104.

1026

1027 Spence, P., O. A. Saenko, M. Eby, and A. J. Weaver, 2009: The Southern Ocean overturning:
1028 Parameterized versus permitted eddies. *J. Phys. Oceanogr.*, **39**, 1634-1651.

1029

1030 Stammer, D., K. Ueyoshi, A. Kohl, W. G. Large, S. A. Josey, and C. Wunsch, 2004: Estimatin-
1031 ing air-sea fluxes of heat, freshwater, and momentum through global ocean data assimilation.
1032 *J. Geophys. Res.*, **109**, C05023, doi:10.1029/2003JC002082.

1033

1034 Steele M., R. Morley, and W. Ermold, 2001: PHC: A global ocean hydrography with a high
1035 quality Arctic Ocean. *J. Clim.*, **14**, 2079-2087.

1036

1037 Talley, L.D., 1996: Antarctic Intermediate Water in the South Atlantic. *The South Atlantic:
1038 Present and Past Circulation*, ed. G. Wefer, W.H. Berger, G. Siedler and D. Webb, Springer-
1039 Verlag, 219-238.

1040

1041 Talley, L. D., 1999: Some aspects of ocean heat transport by the shallow, intermediate and
1042 deep overturning circulations. *Mechanisms of Global Climate Change at Millennial Time
1043 Scales*, Geophys. Monogr., Vol. 112, Amer. Geophys. Union, 1-22.

1044

1045 Talley, L. D., 2003: Shallow, intermediate, and deep over- turning components of the global
1046 heat budget. *J. of Phys. Oceanogr.*, **33**, 530-560.

1047

1048 Talley, L. D., 2007: Hydrographic atlas of the World Ocean Circulation Experiment (WOCE).
1049 Volume 2: Pacific Ocean. Eds. M. Sparrow, P. Chapman and J. Gould. International WOCE
1050 Project Office, Southampton, U.K. 327 pp. <http://www-pord.ucsd.edu/whpatlas/pacific-index.html>

1051

1052 Talley, L. D., 2008: Freshwater transport estimates and the global overturning circulation:
1053 Shallow, deep and throughflow components. *Progr. Oceanogr.*, **78**, 257-303, doi:10.1016/
1054 j.pocean.2008.05.001.

1055

1056 Talley, L. D., T. Chereskin, J. Holte, and Y.-D. Lenn, 2006: Subantarctic Mode Water and
1057 Antarctic Intermediate Water formation near the Subantarctic Front in the southeast Pacific
1058 in winter 2005. Ocean Sciences. Invited abstract, session OS075.

1059

1060 Talley, L. D., J. L. Reid, and P. E. Robbins, 2003. Data-based meridional overturning
1061 streamfunctions for the global ocean. *J. Clim.*, **16**, 3213-3226.

1062

1063 Taylor, P. K., Ed., 2000: Intercomparison and validation of ocean-atmosphere energy flux
1064 fields - Final report of the Joint WCRP/SCOR Working Group on Air-Sea Fluxes. WCRP-
1065 112, WMO/TD-1036, 306 pp.

1066

1067 Thompson R. O. and R. J. Edwards, 1981: Mixing and water mass formation in the Aus-
1068 tralian Sub-Antarctic. *J. Phys. Oceanogr.*, **11**, 1399-1406.

1069

1070 Tsuchiya, M. and L. D. Talley, 1998: A Pacific hydrographic section at 88°W: water property
1071 distribution. *J. Geophys. Res.*, **103**, 12899-12918.

1072

1073 Tsuchiya, M., L.D. Talley and M.S. McCartney, 1994: Water mass distributions in the west-
1074 ern Atlantic: a section from South Georgia Island (54S) northward across the equator. *J.*
1075 *Mar. Res.*, **52**, 55-81.

1076

1077 Tziperman, E., 1986: On the role of interior mixing and air-sea fluxes in determining the

- 1078 stratification and circulation of the oceans. *J. Phys. Oceanogr.*, **16**, 680693.
- 1079
- 1080 Walin, G., 1982: On the relation between sea-surface heat flow and thermal circulation in
1081 the ocean. *Tellus*, **34**, 187-195.
- 1082
- 1083 Warren, B. A., J. H. LaCasce, and P. E. Robbins, 1996: On the obscurantist physics of "form
1084 drag" in theorizing about the Circumpolar Current. *J. Phys. Oceanogr.*, **26**, 2297-2301.
- 1085
- 1086 Willey, D. A., R. A. Fine, R. E. Sonnerup, J. L. Bullister, W. M. Smethie, and M. J.
1087 Warner, 2004: Global oceanic chlorofluorocarbon inventory. *Geophys. Res. Lett.*, **31**,
1088 L01303, doi:10.1029/2003GL018816.
- 1089
- 1090 Wong, A. P. S., 2005: Subantarctic mode water and antarctic intermediate water in the
1091 South Indian Ocean based on profiling float data 2000-2004. *J. Mar. Res.*, **63**, 789-812.
- 1092
- 1093 Wunsch, C. and P. Heimbach, 2007: Practical global ocean state estimation. *Physica D*,
1094 **230**,197-208, doi:10.1016/j.physd.2006.09.040.
- 1095
- 1096 Zhang, H.-M. and L. D. Talley, 1998: Heat and buoyancy budgets and mixing rates in the
1097 upper thermocline of the Indian and Global Oceans. *J. Phys. Oceanogr.*, **28**, 1961-1978.
- 1098

1099 **Figure captions**

1100 Figure 1. SOSE air-sea heat flux (a-c), freshwater heat-equivalent flux from Eq. (1) (d-
 1101 f), and buoyancy heat-equivalent flux (g-i) given by their sum, time averaged for years 2005
 1102 (left), 2006 (middle) and over the time period 2005-2006 (right), all in Wm^{-2} . Positive fluxes
 1103 imply a decrease in surface density (increase in surface buoyancy). The color contours are
 1104 climatological positions of the fronts given by Orsi et al. (1995): Subtropical Front (STF,
 1105 black), Subantarctic Front (SAF, red), Polar Front (PF, green) and Southern ACC front
 1106 (SACC, blue).

1107

1108 Figure 2. Time-mean surface density (in σ_θ units, contours) and buoyancy heat-equivalent
 1109 flux (in Wm^{-2} , color shading), averaged for years 2005-2006, obtained by (a) SOSE, (b)
 1110 NCEP1, (c) ECMWF Reanalysis (ERA-Interim), (d) LY09 and (e) OCCA. Color contours
 1111 are as in Figure 1.

1112

1113 Figure 3. Potential vorticity given by Eq. (9) ($10^{-12}/(\text{m-s})$), on constant σ_θ surfaces
 1114 ranging from 26.50 to 26.75 (panels a-f) with the contour increment of 0.05, averaged over
 1115 years 2005 and 2006 from SOSE. Black curve is the 300 m contour of September mixed layer
 1116 depth from Dong et al. (2008). Thick line is the climatological position of the Polar Front
 1117 (PF) front given by Orsi et al. (1995).

1118

1119 Figure 4. The same as Figure 3 except showing σ_θ surfaces ranging from 26.80 to 27.05
 1120 (panels a-f).

1121

1122 Figure 5. Isopycnal distribution of depth (m) (a,b), potential temperature ($^\circ$) (c,d) and
 1123 salinity (e,f) averaged over years 2005 and 2006 from SOSE at: (left column) $\sigma_\theta=26.8$ and

1124 (right column) $\sigma_\theta=26.9$. Thick line is the climatological position of the SAF (Orsi et al.,
 1125 1995).

1126

1127 Figure 6. The same as Figure 5 except for $\sigma_\theta=27.0$ and (right column) $\sigma_\theta=27.1$.

1128

1129 Figure 7. Potential vorticity given by Eq. (9) along: (a) 30 °S, (b) 45 °S, (c) 50 °S and
 1130 (d) 58 °S, in units of $10^{-14}/(\text{cm-s})$.

1131

1132 Figure 8. The global ocean (south of 24.7°S) transformation (left) and formation (right)
 1133 rates (Sv) from five-day averaged SOSE heat flux (HF - positive values correspond to ocean
 1134 heat loss, ocean density increase), freshwater heat-equivalent flux (FWF - positive values
 1135 correspond to freshwater loss by evaporation, ocean density increase) and buoyancy heat-
 1136 equivalent flux (shown in Figure 1, BF) and sea surface density, subsequently averaged over
 1137 years 2005 (top), 2006 (middle) and 2005-2006 (bottom). A positive transformation rate
 1138 corresponds to conversion of light water into denser water across a given isopycnal σ_θ . Dark
 1139 vertical lines mark the σ_θ values of southeast Indian SAMW (26.8) and southeast Pacific
 1140 SAMW (27.0); light vertical lines show the limits of the corresponding outcrop windows,
 1141 each 0.1 σ_θ wide.

1142

1143 Figure 9. Transformation (left) and formation (right) rates (Sv), using five-day averaged
 1144 SOSE buoyancy heat-equivalent flux (whose annual average is shown in Figure 1) and sea
 1145 surface density for 2005 (top), 2006 (middle), and average over both years (bottom), as in
 1146 Figure 8. Shown are the estimates for the global ocean south of 24.7°S as well as for the
 1147 three individual ocean basins: Pacific, Indian and Atlantic, where transports through the lat-
 1148 eral sides of each ocean region in the uppermost layer of SOSE have been taken into account.

1149

1150 Figure 10. Monthly mean estimates of transformation (left) and formation (right) (Sv),
 1151 using SOSE five-day averaged buoyancy flux (shown in Figure 1) and sea surface density.
 1152 Estimates are for the global ocean south of 24.7°S, time-averaged for 2005 and 2006. Red
 1153 curves show transformation and formation rates averaged over 2005-2006, identical to the
 1154 black curves in Figure 8e,f.

1155

1156 Figure 11. Average transformation rates for SEISAMW [$\sigma_\theta=26.75$ (left) and $\sigma_\theta=26.85$,
 1157 in Sv m^{-2} (right)] for 2005-2006 for October through March (top), April through Septem-
 1158 ber (middle), and the annual average (bottom). Positive values indicate that the water is
 1159 becoming denser. The black lines are the 300 m contour of September mixed layer depths
 1160 from Dong et al. (2008) and the gray line is the climatological position of the SAF (Orsi et
 1161 al., 1995).

1162

1163 Figure 12. The same as Figure 11 except for SEPSAMW: $\sigma_\theta=26.95$ (left) and 27.05
 1164 (right).

1165

1166 Figure 13. Average formation rates for SEISAMW ($\sigma_\theta=26.8$) (left) and SEPSAMW
 1167 ($\sigma_\theta=27.05$) (right), in Sv m^{-2} , for October to March (top), April to September (middle),
 1168 and the annual average (bottom). These maps are obtained by subtracting the transforma-
 1169 tion rate maps shown in Figures 11 ($\sigma_\theta=26.85$ minus $\sigma_\theta=26.75$) and 12 ($\sigma_\theta=27.05$ minus
 1170 $\sigma_\theta=26.95$), respectively. The black and gray curves are as in Figure 11.

1171

1172 Figure 14. Meridional volume transport (Sv) across 30 °S (panels a-d), zonal transport
 1173 between the individual ocean sectors (e-g) and storage rate (h-k) for period 2005-2006. Note
 1174 different scales in panels a-d and e-k. Positive transport is northward in panels a-d and
 1175 eastward in panels e-g. The longitude bounds are: 150°E-70°W for the Pacific sector, 70°W-

1176 20°E for the Atlantic sector and 20°E-150°E for the Indian sector.

1177

1178 Figure 15. Average (2005-2006) net transports south of 30 °S in isopycnal layers 0.1
1179 kg/m³ wide for (a) Indian, (b) South Pacific, (c) South Atlantic and (d) Southern Ocean
1180 (sum of all sectors), showing zonal transport (Sv) in and out of each ocean sector, meridional
1181 transport (Sv) through 30 °S, formation by air-sea buoyancy fluxes estimated from Walin
1182 analysis, and the residual transport, which is ascribed to the effects of diapycnal mixing on
1183 volume balance in that isopycnal layer; colors are indicated in the legend. Positive trans-
1184 ports are transports into ocean basin and negative transports are out of the ocean basin. The
1185 storage term is $-dV/dt$ where V is total volume, plotted with a negative sign to emphasize
1186 the full balance of terms. The budget is estimated from Eq. (7).

1187

1188 Appendix: Figure A1. Transformation (left) and formation (right) rates, in Sv, as in
1189 Figure 8 except based on NCEP1, ERA, LY09 and OCCA buoyancy heat equivalent flux
1190 and sea surface density, each estimated using five-day averages and subsequently averaged
1191 over year 2005 (left) and 2006 (right). SOSE and OCCA provide all the variables, including
1192 sea surface salinity, needed to estimate the air-sea buoyancy flux. For NCEP1 and ERA,
1193 sea surface salinity from the NCEP Global Ocean Data Assimilation System was used. For
1194 LY09, sea surface salinity from the Polar Science Center Hydrographic Climatology (PHC2)
1195 was used (see Section 6).

1196

1197 Table captions

1198 Table 1: Time averaged (2005-2006) meridional volume transport estimates (in Sv) across
 1199 30 °S from SOSE compared with Talley (2003) and Iudicone et al. (2008a).

1200

1201 Table 2: a) SAMW volume budget (in Sv) for σ_θ range 26.5-27.1 kg/m³ in each ocean
 1202 sector for years 2005 (first entry) and 2006 (second entry). b) SAMW volume budget for σ_θ
 1203 range 26.7-27.1 kg/m³ in each ocean sector.

1204

1205 Table 3: The same as Table 2, but for narrow density ranges characteristic of the more
 1206 pronounced SAMWs, and within individual ocean sectors. Volume budget (in Sv) for
 1207 southeast Indian SAMW (SEISAMW, Indian sector) (σ_θ range 26.75-26.85 kg/m³), south-
 1208 east Pacific SAMW (SEPSAMW, Pacific sector) (σ_θ range 26.95-27.05 kg/m³) and South
 1209 Atlantic SAMW (Atlantic sector) (σ_θ range 26.55-26.65 kg/m³) for years 2005, 2006.

1210

1211 Appendix:Table A1: Densities σ_θ (center of 0.1 σ_θ interval is listed) and global formation
 1212 rate (\mathcal{FR}) estimates (in Sv), given by Eq. (5), of SEISAMW and SEPSAMW from Walin
 1213 analysis for years 2005 and 2006 using various air-sea flux products, also shown in Figure
 1214 A1c and d.

1215 **7 Figures**

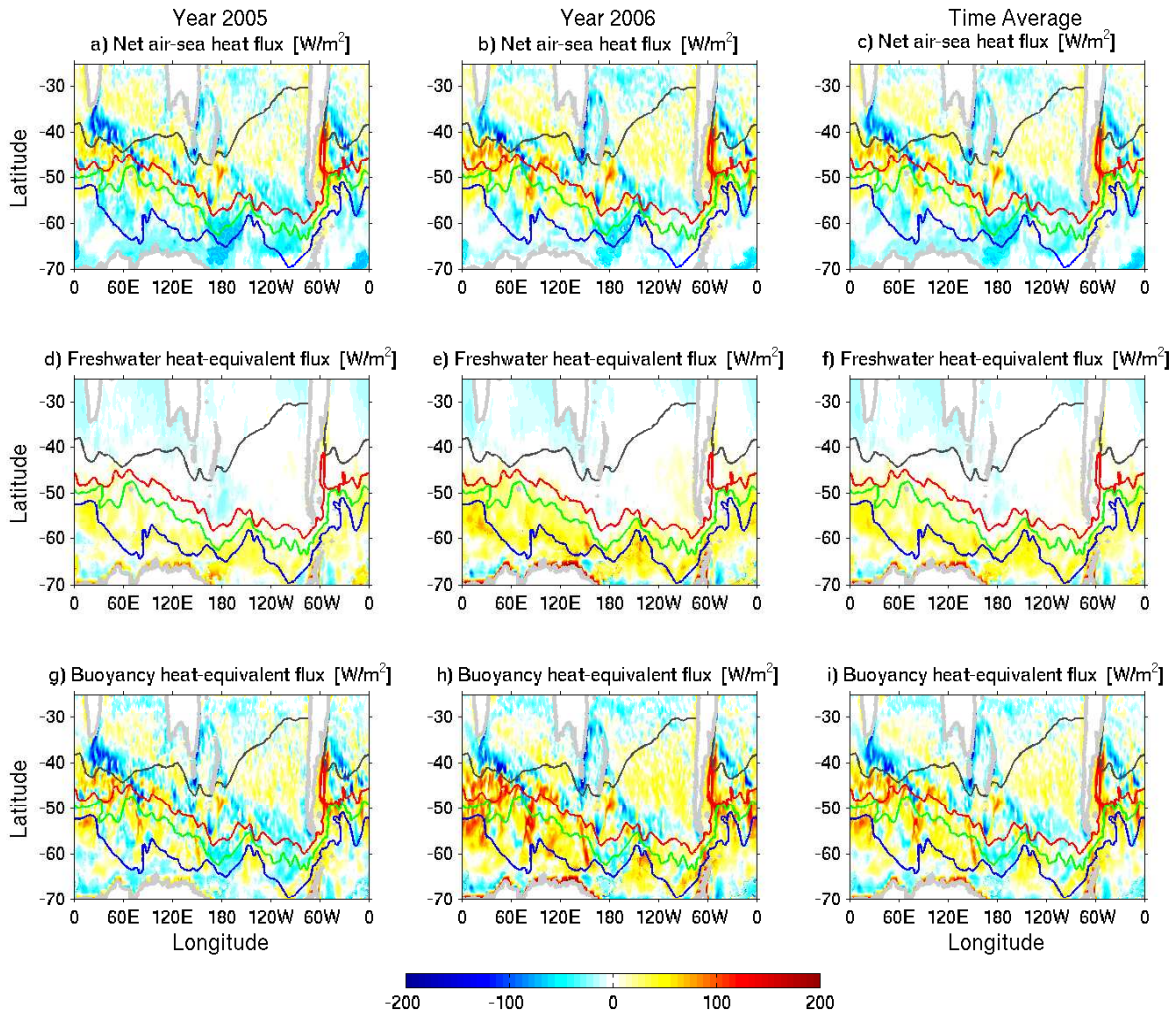


Figure 1: SOSE air-sea heat flux (a-c), freshwater heat-equivalent flux from Eq. (1) (d-f), and buoyancy heat-equivalent flux (g-i) given by their sum, time averaged for years 2005 (left), 2006 (middle) and over the time period 2005-2006 (right), all in Wm^{-2} . Positive fluxes imply a decrease in surface density (increase in surface buoyancy). The color contours are climatological positions of the fronts given by Orsi et al. (1995): Subtropical Front (STF, black), Subantarctic Front (SAF, red), Polar Front (PF, green) and Southern ACC front (SACC, blue).

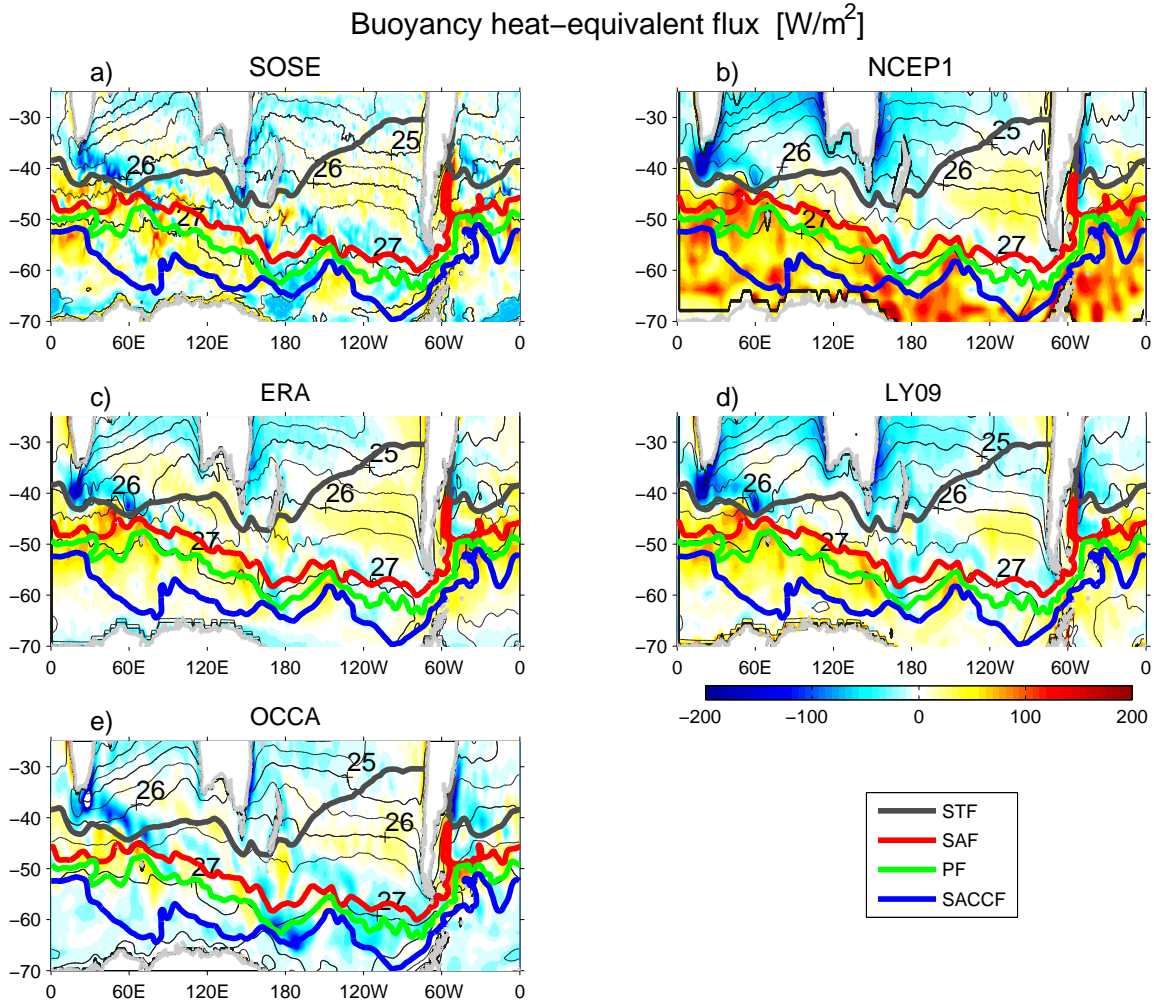


Figure 2: Time-mean surface density (in σ_θ units, contours) and buoyancy heat-equivalent flux (in Wm^{-2} , color shading), averaged for years 2005-2006, obtained by (a) SOSE, (b) NCEP1, (c) ECMWF Reanalysis (ERA-Interim), (d) LY09 and (e) OCCA. Color contours are as in Figure 1.

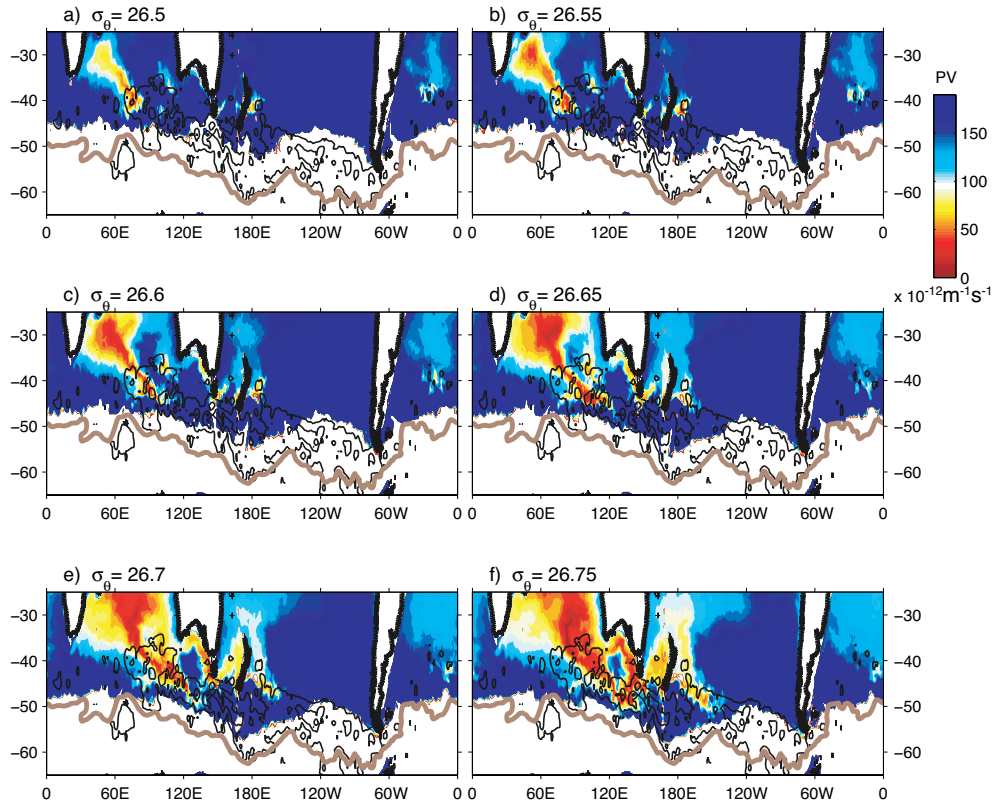


Figure 3: Potential vorticity given by Eq. (9) ($10^{-12}/(\text{m}\cdot\text{s})$), on constant σ_θ surfaces ranging from 26.50 to 26.75 (panels a-f) with the contour increment of 0.05, averaged over years 2005 and 2006 from SOSE. Black curve is the 300 m contour of September mixed layer depth from Dong et al. (2008). Thick line is the climatological position of the Polar Front (PF) front given by Orsi et al. (1995).

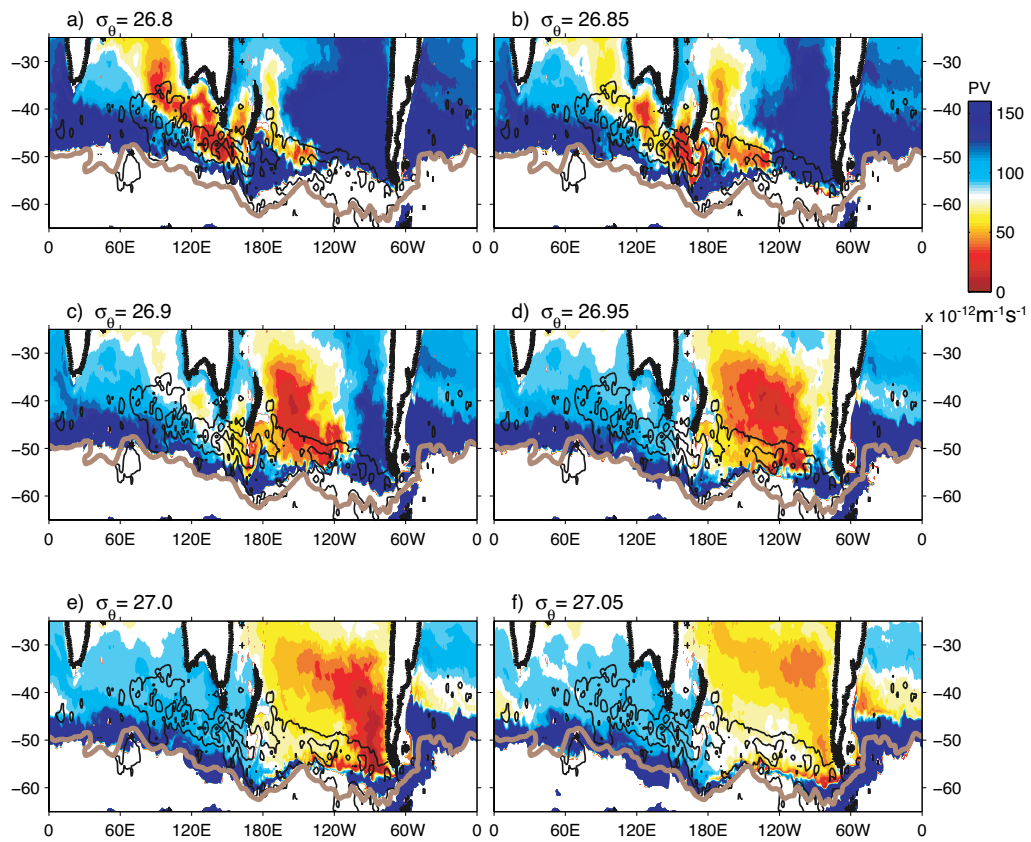


Figure 4: The same as Figure 3 except showing σ_θ surfaces ranging from 26.80 to 27.05 (panels a-f).

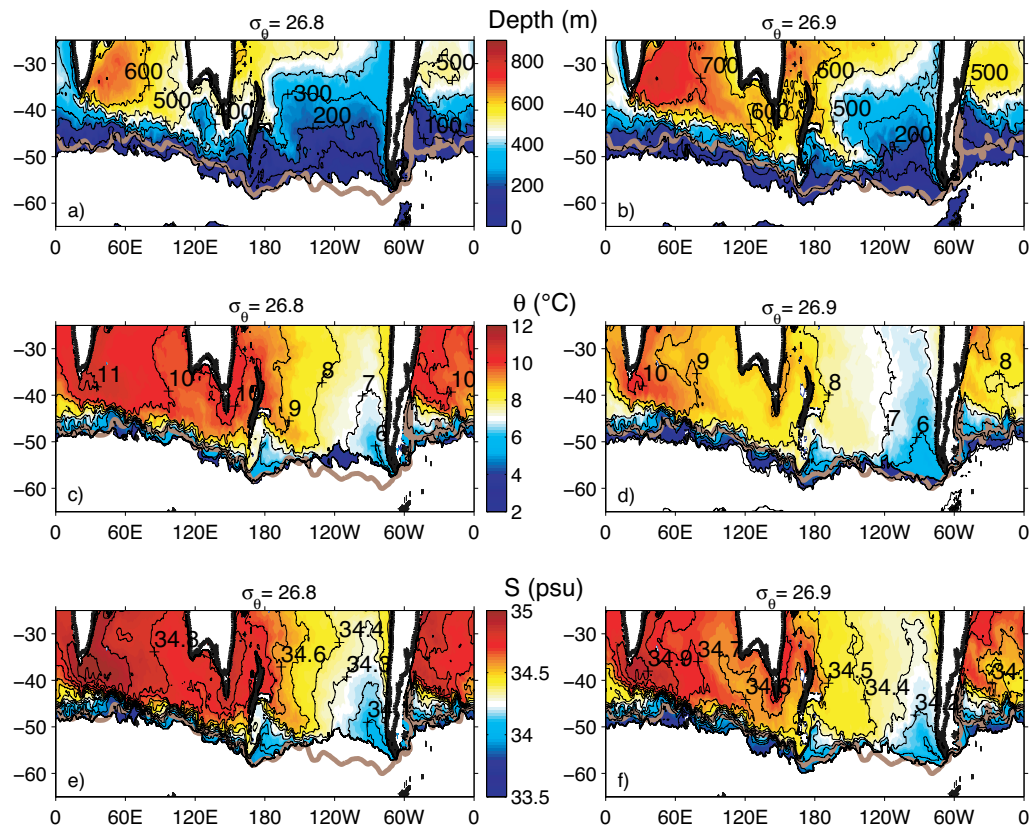


Figure 5: Isopycnal distribution of depth (m) (a,b), potential temperature ($^\circ$) (c,d) and salinity (e,f) averaged over years 2005 and 2006 from SOSE at: (left column) $\sigma_\theta=26.8$ and (right column) $\sigma_\theta=26.9$. Thick line is the climatological position of the SAF (Orsi et al., 1995).

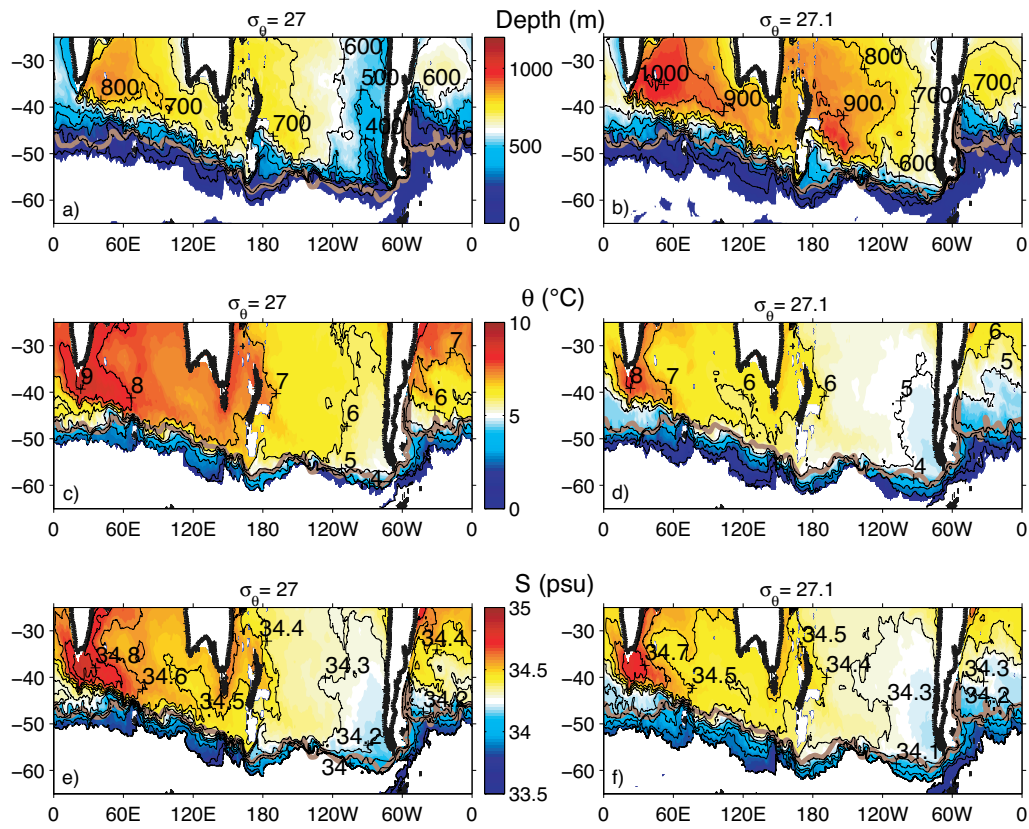


Figure 6: The same as Figure 5 except for $\sigma_\theta=27.0$ and (right column) $\sigma_\theta=27.1$.

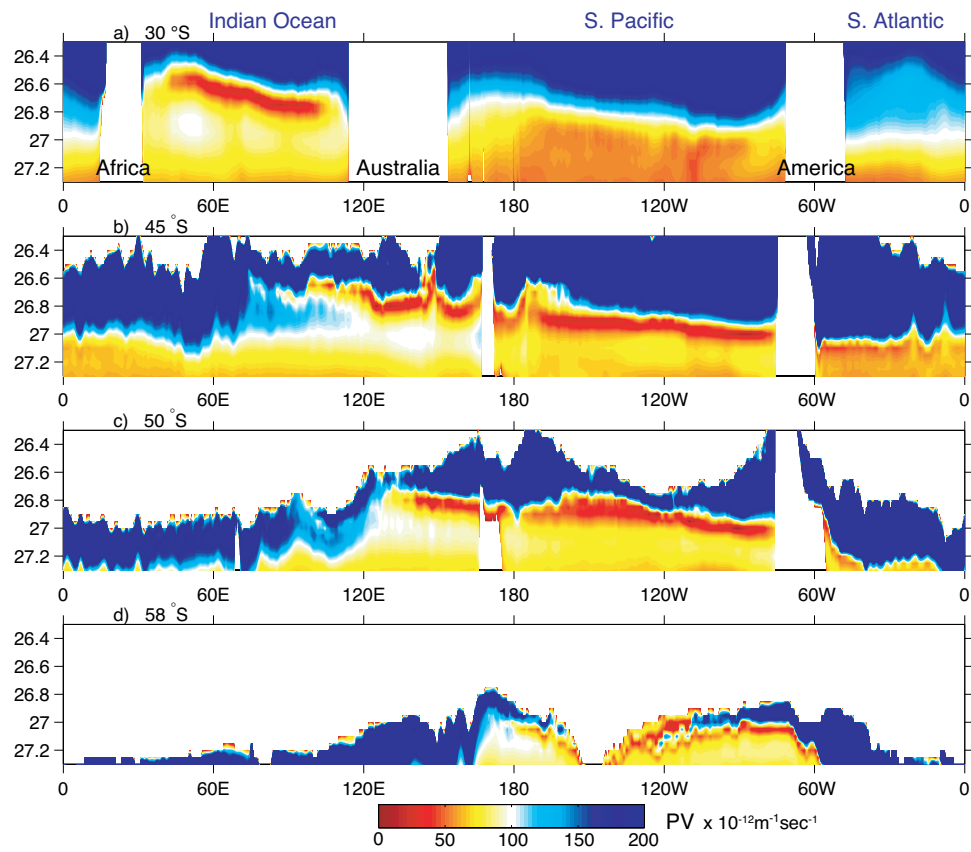


Figure 7: Potential vorticity given by Eq. (9) along: (a) 30 °S, (b) 45 °S, (c) 50 °S and (d) 58 °S, in units of $10^{-14}/(\text{cm}\cdot\text{s})$.

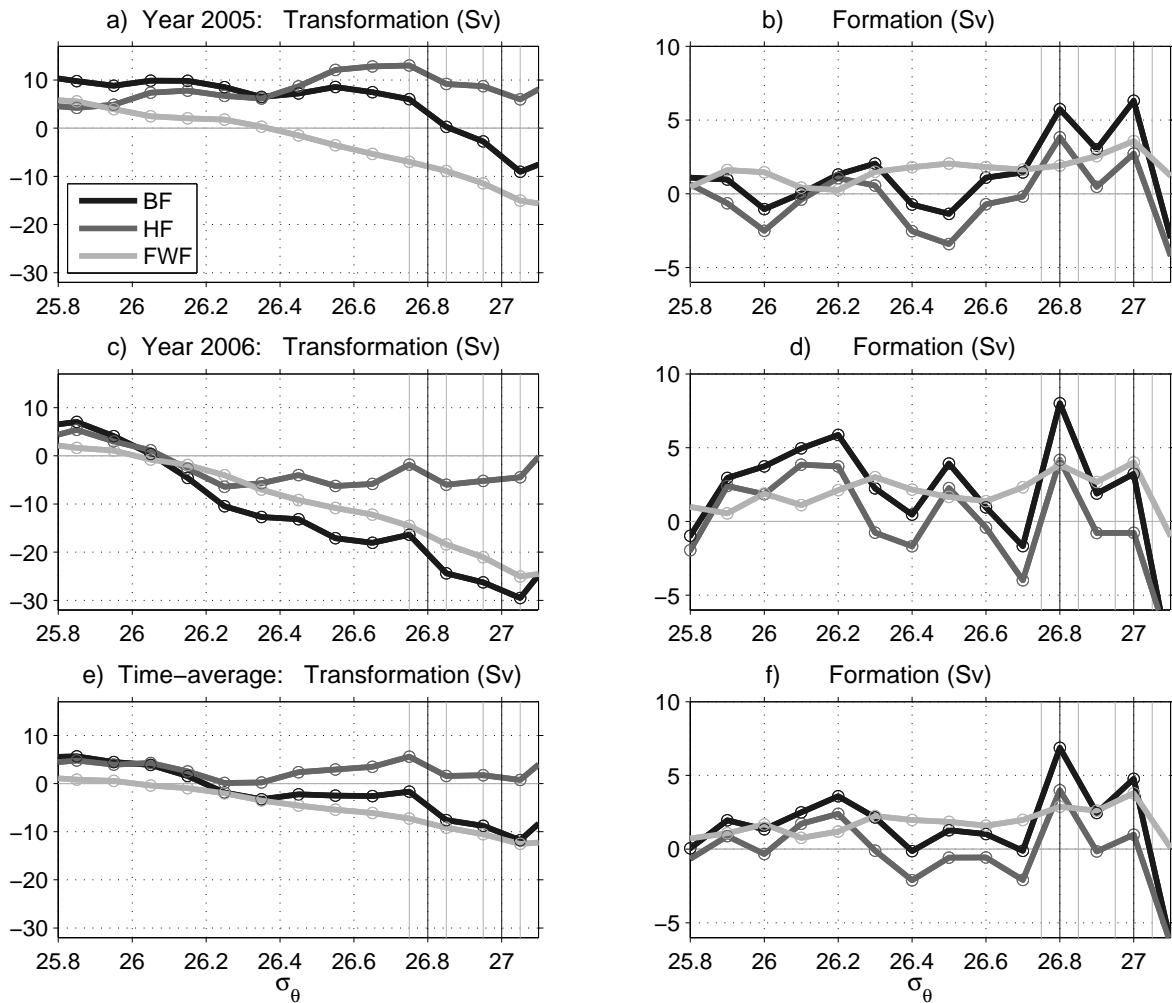


Figure 8: The global ocean (south of 24.7°S) transformation (left) and formation (right) rates (Sv) from five-day averaged SOSE heat flux (HF - positive values correspond to ocean heat loss, ocean density increase), freshwater heat-equivalent flux (FWF - positive values correspond to freshwater loss by evaporation, ocean density increase) and buoyancy heat-equivalent flux (shown in Figure 1, BF) and sea surface density, subsequently averaged over years 2005 (top), 2006 (middle) and 2005-2006 (bottom). A positive transformation rate corresponds to conversion of light water into denser water across a given isopycnal σ_θ . Dark vertical lines mark the σ_θ values of southeast Indian SAMW (26.8) and southeast Pacific SAMW (27.0); light vertical lines show the limits of the corresponding outcrop windows, each $0.1 \sigma_\theta$ wide.

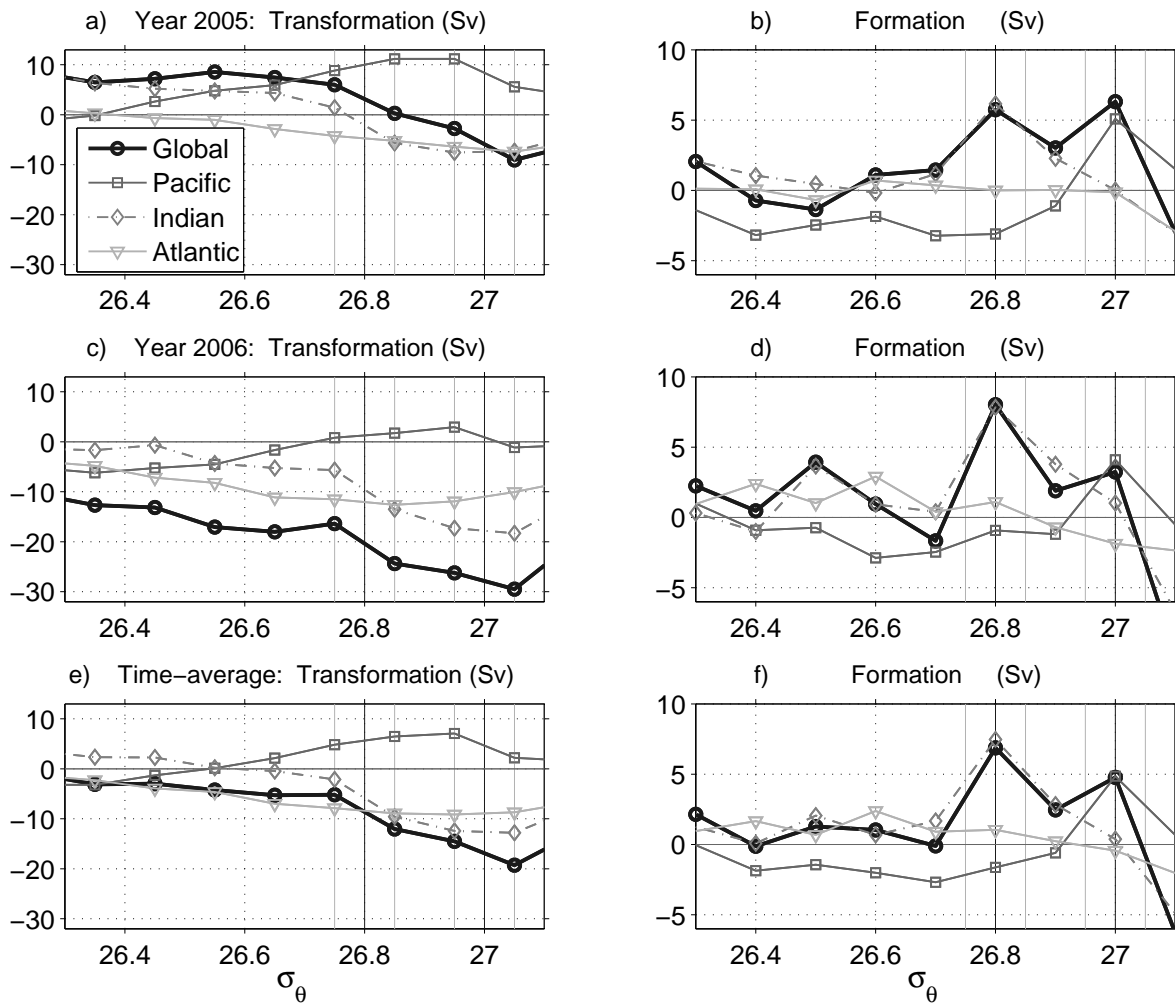


Figure 9: Transformation (left) and formation (right) rates (Sv), using five-day averaged SOSE buoyancy heat-equivalent flux (whose annual average is shown in Figure 1) and sea surface density for 2005 (top), 2006 (middle), and average over both years (bottom), as in Figure 8. Shown are the estimates for the global ocean south of 24.7°S as well as for the three individual ocean basins: Pacific, Indian and Atlantic, where transports through the lateral sides of each ocean region in the uppermost layer of SOSE have been taken into account.

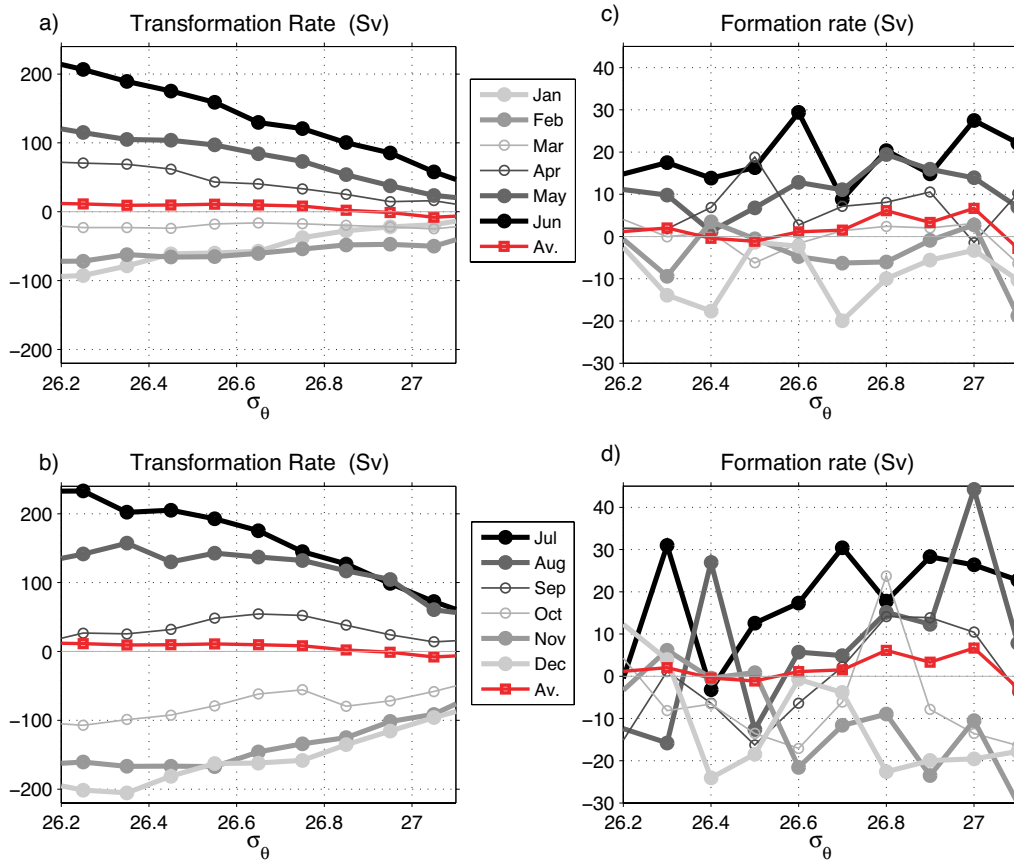


Figure 10: Monthly mean estimates of transformation (left) and formation (right) (Sv), using SOSE five-day averaged buoyancy flux (shown in Figure 1) and sea surface density. Estimates are for the global ocean south of 24.7°S, time-averaged for 2005 and 2006. Red curves show transformation and formation rates averaged over 2005-2006, identical to the black curves in Figure 8e,f.

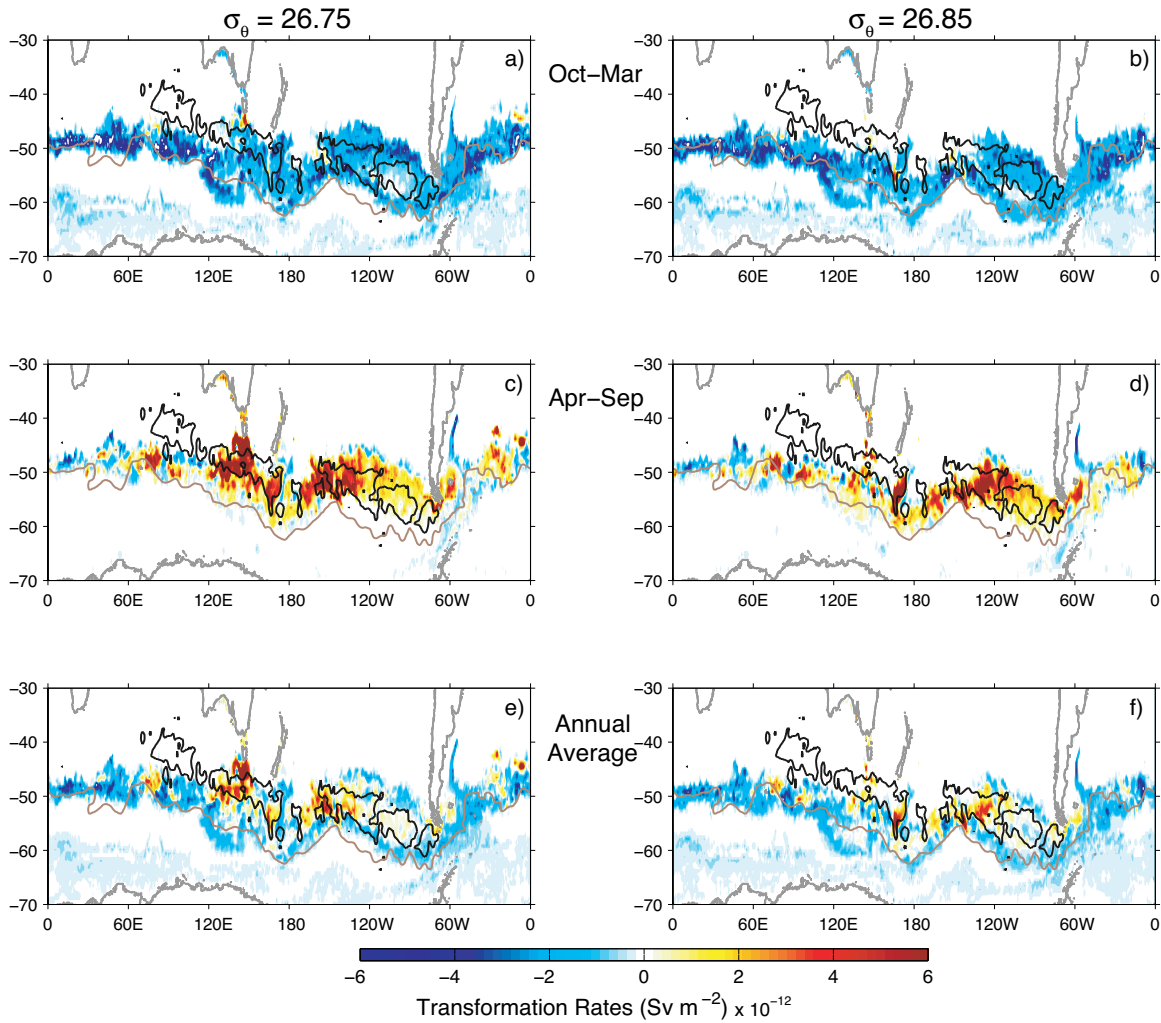


Figure 11: Average transformation rates for SEISAMW [$\sigma_\theta=26.75$ (left) and $\sigma_\theta=26.85$, in Sv m^{-2} (right)] for 2005-2006 for October through March (top), April through September (middle), and the annual average (bottom). Positive values indicate that the water is becoming denser. The black lines are the 300 m contour of September mixed layer depths from Dong et al. (2008) and the gray line is the climatological position of the SAF (Orsi et al., 1995).

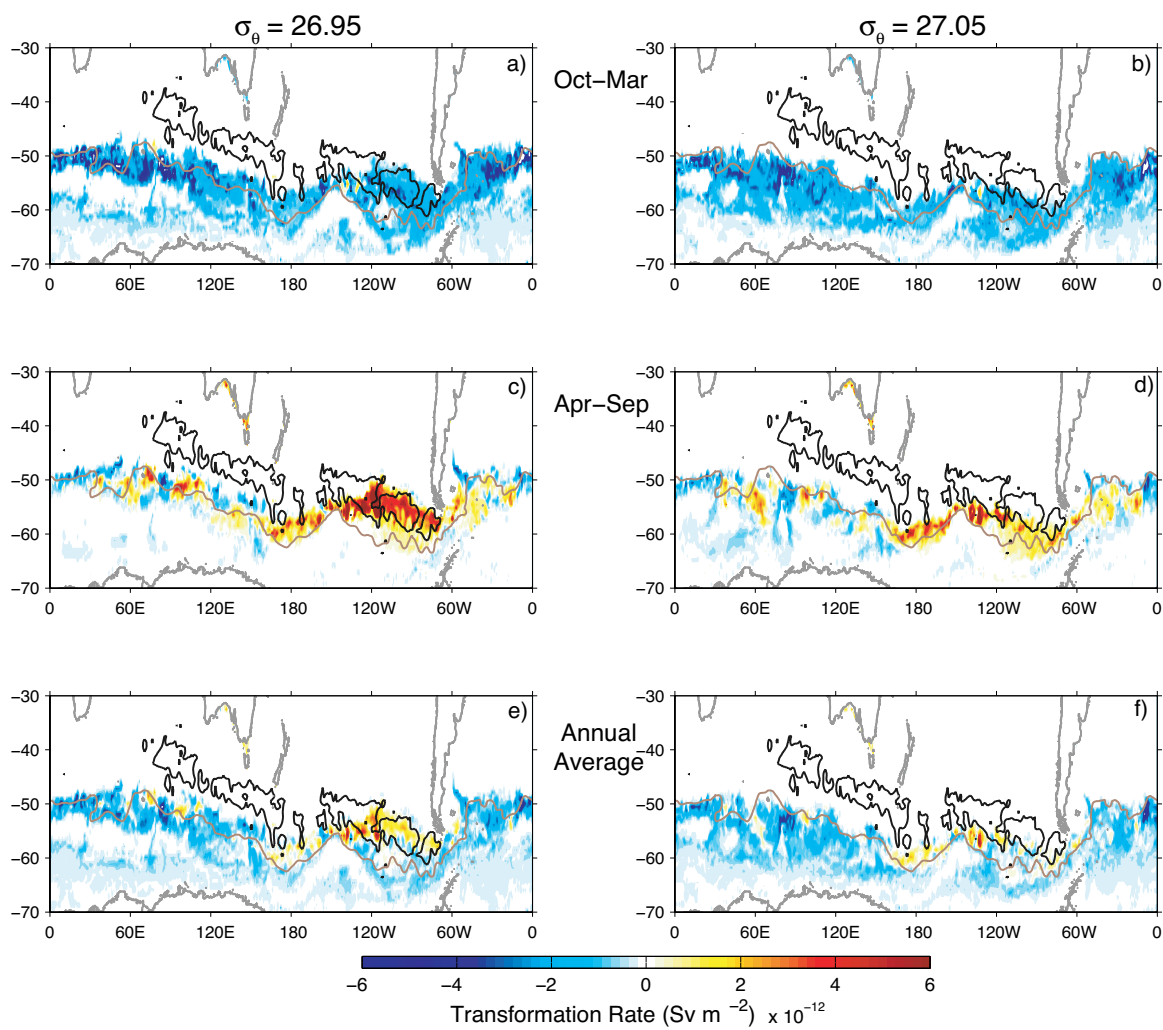


Figure 12: The same as Figure 11 except for SEPSAMW: $\sigma_\theta=26.95$ (left) and 27.05 (right).

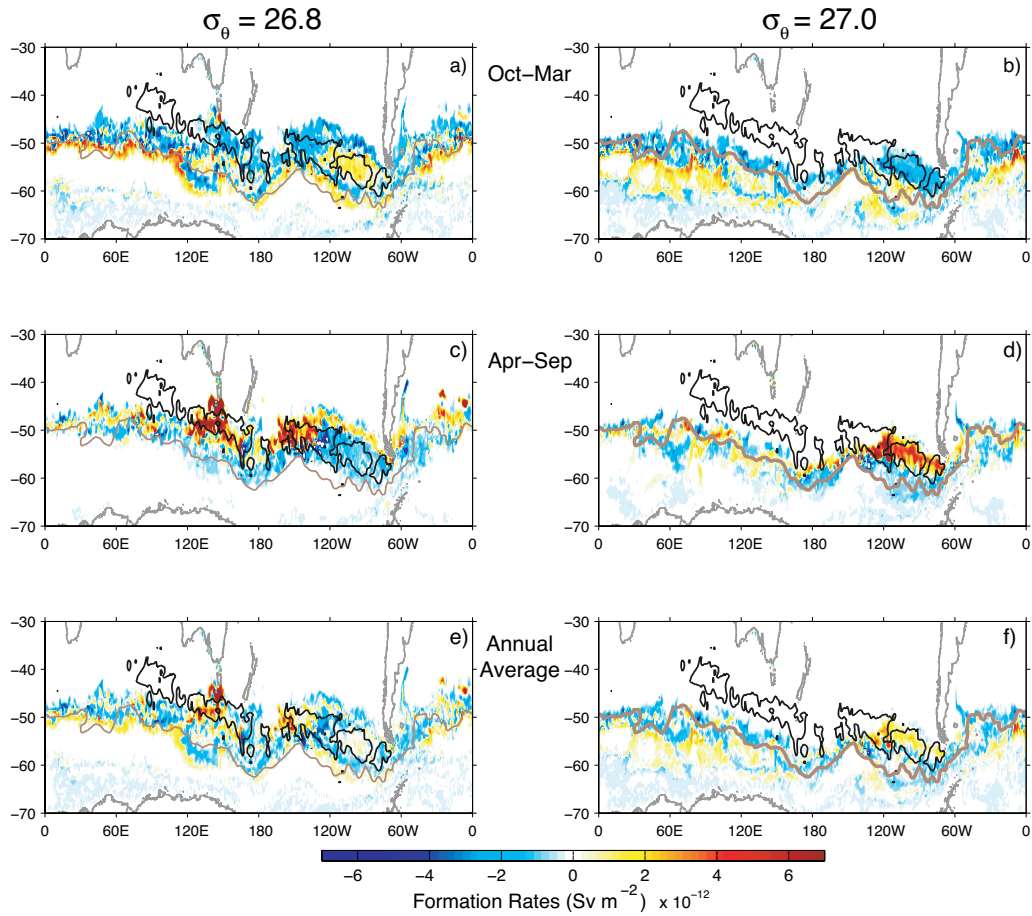


Figure 13: Average formation rates for SEISAMW ($\sigma_\theta=26.8$) (left) and SEPSAMW ($\sigma_\theta=27.05$) (right), in Sv m^{-2} , for October to March (top), April to September (middle), and the annual average (bottom). These maps are obtained by subtracting the transformation rate maps shown in Figures 11 ($\sigma_\theta=26.85$ minus $\sigma_\theta=26.75$) and 12 ($\sigma_\theta=27.05$ minus $\sigma_\theta=26.95$), respectively. The black and grey curves are as in Figure 11.

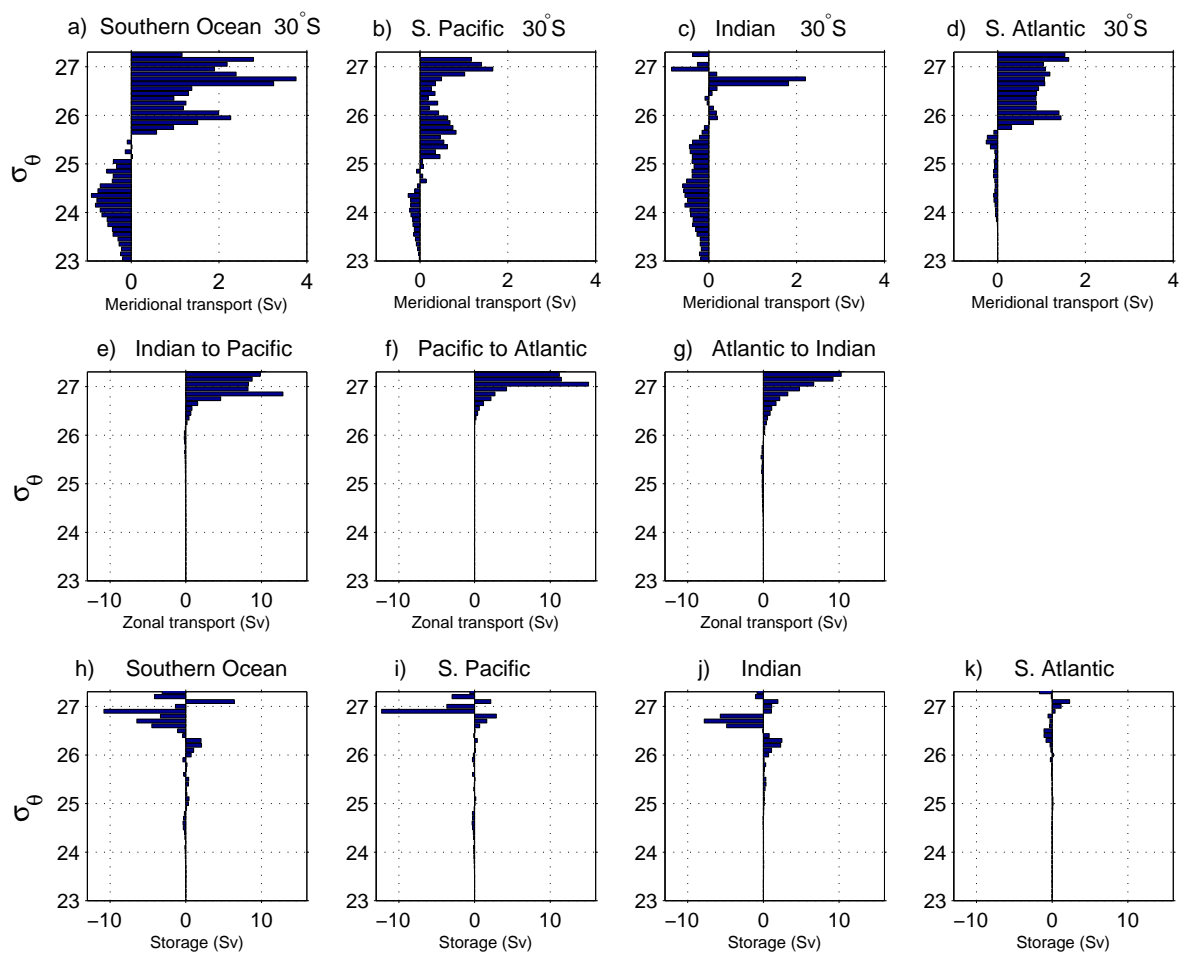


Figure 14: Meridional volume transport (Sv) across 30°S (panels a-d), zonal transport between the individual ocean sectors (e-g) and storage rate (h-k) for period 2005-2006. Note different scales in panels a-d and e-k. Positive transport is northward in panels a-d and eastward in panels e-g. The longitude bounds are: 150°E-70°W for the Pacific sector, 70°W-20°E for the Atlantic sector and 20°E-150°E for the Indian sector.

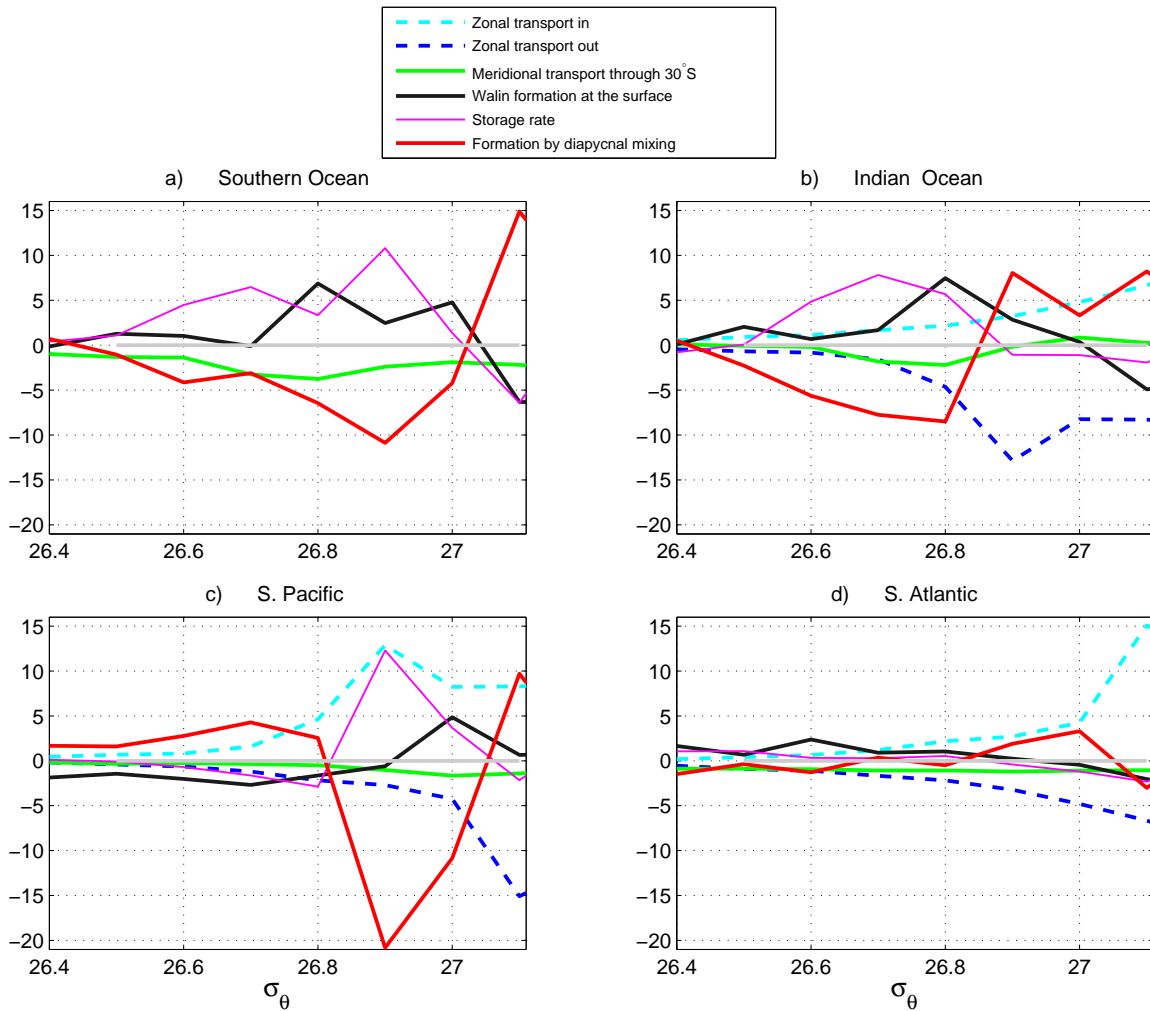


Figure 15: Average (2005-2006) net transports south of 30 °S in isopycnal layers 0.1 kg/m³ wide for (a) Indian, (b) South Pacific, (c) South Atlantic and (d) Southern Ocean (sum of all sectors), showing zonal transport (Sv) in and out of each ocean sector, meridional transport (Sv) through 30 °S, formation by air-sea buoyancy fluxes estimated from Walin analysis, and the residual transport, which is ascribed to the effects of diapycnal mixing on volume balance in that isopycnal layer; colors are indicated in the legend. Positive transports are transports into ocean basin and negative transports are out of the ocean basin. The storage term is $-dV/dt$ where V is total volume, plotted with a negative sign to emphasize the full balance of terms. The budget is estimated from Eq. (7).

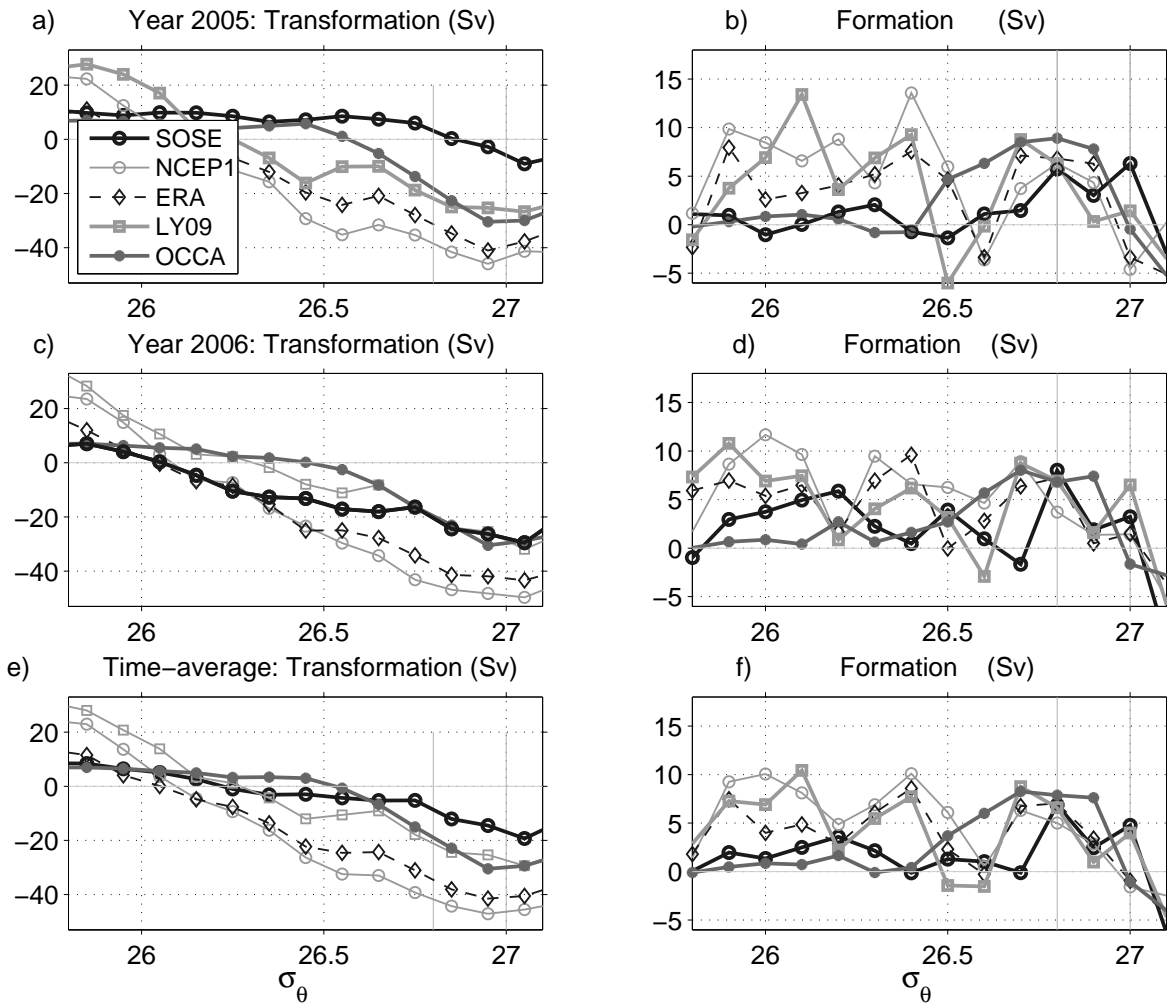


Figure 16: Appendix Figure A1. Transformation (left) and formation (right) rates, in Sv, as in Figure 8 except based on NCEP1, ERA, LY09 and OCCA buoyancy heat equivalent flux and sea surface density, each estimated using five-day averages and subsequently averaged over year 2005 (left) and 2006 (right). SOSE and OCCA provide all the variables, including sea surface salinity, needed to estimate the air-sea buoyancy flux. For NCEP1 and ERA, sea surface salinity from the NCEP Global Ocean Data Assimilation System was used. For LY09, sea surface salinity from the Polar Science Center Hydrographic Climatology (PHC2) was used (see Section 6). (Note to JPO editor: latex automatically numbered this as Figure 16. It is Figure A1.)

1216 **8 Tables**

1217 Table 1: Time averaged (2005-2006) meridional volume transport estimates (in Sv) across
 1218 30 °S from SOSE compared with Talley (2003) and Iudicone et al. (2008a).

Ocean sector	density range	Talley (2003) transports	SOSE transports	Iudicone et al. (2008a,c) transports
Pacific	$26.7 < \sigma_{\theta} < 27.0$	2.2	4.6	
Atlantic	$26.7 < \sigma_{\theta} < 27.0$	4.1	4.4	
Indian	$26.7 < \sigma_{\theta} < 26.89$	1.5	1.5	
Indian	$26.89 < \sigma_{\theta} < 27.0$	-1.5	-1.1	
Pacific	$26.0 < \sigma_{\theta} < 27.2$		7.9	7.2
Atlantic	$26.0 < \sigma_{\theta} < 27.2$		14.5	9.5
Indian	$26.0 < \sigma_{\theta} < 27.2$		3.1	2.7

1220 Table 2: a) SAMW volume budget (in Sv) for σ_θ range 26.5-27.1 kg/m³ in each ocean
 1221 sector for years 2005 (first entry) and 2006 (second entry).

Ocean sector	Meridional transport across 30°S (a)	Zonal transport into ocean sector (b)	Zonal transport out of an ocean sector (c)	Formation by air-sea buoyancy fluxes (d)	Storage rate (e)	Formation by diapycnal mixing (a - b + c - d + e)
1222 Indian	3.6, 2.9	29.8, 27.9	45.3, 45.1	9.4, 10.9	-16.3, -12.3	-6.6, -3.1
South Pacific	6.6, 6.1	45.3, 45.1	37.0, 38.0	-1.1, -4.6	-5.0, -12.0	-5.6, -8.4
South Atlantic	7.9, 8.1	37.0, 38.0	29.8, 27.9	5.0, 0.5	2.0, 1.4	-2.3, -1.1
Southern Ocean	18.2, 17.1			13.2, 6.8	-19.3, -22.9	-14.5, -12.6

1223 b) SAMW volume budget for σ_θ range 26.7-27.1 kg/m³ in each ocean sector.

Ocean sector	Meridional transport across 30°S (a)	Zonal transport into ocean sector (b)	Zonal transport out of an ocean sector (c)	Formation by air-sea buoyancy fluxes (d)	Storage rate (e)	Formation by diapycnal mixing (a - b + c - d + e)
1224 Indian	1.5, 1.0	27.2, 25.0	42.8, 42.8	8.5, 6.3	-7.3, -11.5	1.3, 1.0
South Pacific	6.0, 5.5	42.8, 42.8	35.5, 35.9	2.2, -1.0	-5.4, -13.2	-8.9, -13.6
South Atlantic	5.9, 6.1	35.5, 35.9	27.2, 25.0	2.8, -3.4	4.8, 1.4	-0.4, 0.0
Southern Ocean	13.4, 12.6			13.5, 1.9	-7.8, -23.3	-7.9, -12.6

1225 Table 3: The same as Table 2, but for narrow density ranges characteristic of the more
 1226 pronounced SAMWs, and within individual ocean sectors. Volume budget (in Sv) for
 1227 southeast Indian SAMW (SEISAMW, Indian sector) (σ_θ range 26.75-26.85 kg/m³), southeast
 1228 Pacific SAMW (SEPSAMW, Pacific sector) (σ_θ range 26.95-27.05 kg/m³) and South Atlantic
 1229 SAMW (Atlantic sector) (σ_θ range 26.55-26.65 kg/m³) for years 2005, 2006.

Water mass	Meridional transport across 30°S (a)	Zonal transport into ocean sector (b)	Zonal transport out of an ocean sector (c)	Formation by air-sea buoyancy fluxes (d)	Storage rate (e)	Formation by diapycnal mixing (a - b + c - d + e)
SEISAMW	0.3, 0.1	3.7, 2.7	13.0, 12.7	7.1, 7.8	-8.0, -3.3	-5.5, -1.0
SEPSAMW	1.6, 1.2	8.2, 8.4	15.3, 14.9	5.6, 4.1	-2.6, -4.8	0.5, -1.2
S. Atlantic SAMW	1.0, 0.9	1.0, 1.4	1.7, 1.7	1.8, 2.9	-1.0, 0.3	-1.1, -1.4

1231 Table A1: Densities σ_θ (center of 0.1 σ_θ interval is listed) and global formation rate (\mathcal{FR})
 1232 estimates (in Sv), given by Eq. (5), of SEISAMW and SEPSAMW from Walin analysis for
 1233 years 2005 and 2006 using various air-sea flux products, also shown in Figure A1c and d.

Data source	SEISAMW: σ_θ and \mathcal{FR} , yr 2005		SEPSAMW: σ_θ and \mathcal{FR} , yr 2005		SEISAMW: σ_θ and \mathcal{FR} , yr 2006		SEPSAMW: σ_θ and \mathcal{FR} , yr 2006	
SOSE	26.8	5.6 Sv	27.0	6.3 Sv	26.8	8.2 Sv	27.0	3.2 Sv
NCEP1	26.8	6.2 Sv	26.9	4.2 Sv	26.7	8.9 Sv	27.0	1.4 Sv
ECMWF	26.7	6.9 Sv	27.0	6.2 Sv	26.8	7.2 Sv	27.0	1.6 Sv
LY09	26.7	8.8 Sv	27.0	1.4 Sv	26.7	8.7 Sv	27.0	6.5 Sv
OCCA	26.8	8.9 Sv	26.9	7.8 Sv	26.7	8.0 Sv	26.9	7.4 Sv

1234